ARTICLE IN PRESS

Nature Communications

https://doi.org/10.1038/s41467-026-69432-x

Article in Press

Coupling programmable shape morphing and solvent-fueled propulsion in a soft bicontinuous composite

Received: 28 July 2025

Accepted: 2 February 2026

Cite this article as: Giri, P., Borbora, A., Sarkar, D. *et al.* Coupling programmable shape morphing and solvent-fueled propulsion in a soft bicontinuous composite. *Nat Commun* (2026). https://doi.org/10.1038/s41467-026-69432-x

Pritam Giri, Angana Borbora, Debasmita Sarkar, Sayonti Dutta, Alan H. Weible, Hrisikesh Sarma, Arijit Mohanta, Xiaoguang Wang & Uttam Manna

We are providing an unedited version of this manuscript to give early access to its findings. Before final publication, the manuscript will undergo further editing. Please note there may be errors present which affect the content, and all legal disclaimers apply.

If this paper is publishing under a Transparent Peer Review model then Peer Review reports will publish with the final article.

ARTICLE IN PRESS

© The Author(s) 2026. **Open Access** This article is licensed under a Creative Commons Attribution-NonCommercial-NoDerivatives 4.0 International License, which permits any non-commercial use, sharing, distribution and reproduction in any medium or format, as long as you give appropriate credit to the original author(s) and the source, provide a link to the Creative Commons licence, and indicate if you modified the licensed material. You do not have permission under this licence to share adapted material derived from this article or parts of it. The images or other third party material in this article are included in the article's Creative Commons licence, unless indicated otherwise in a credit line to the material. If material is not included in the article's Creative Commons licence and your intended use is not permitted by statutory regulation or exceeds the permitted use, you will need to obtain permission directly from the copyright holder. To view a copy of this licence, visit http://creativecommons.org/licenses/by-nc-nd/4.0/.

ARTICLE IN PRESS

Coupling programmable shape morphing and solvent-fueled propulsion in a soft bicontinuous composite

Pritam Giri,[1] Angana Borbora,[2] Debasmita Sarkar,[2] Sayonti Dutta,[2] Alan H. Weible,[3] Hrisikesh Sarma,[2] Arijit Mohanta,[4] Xiaoguang Wang[3,5]* and Uttam Manna[1,2,6]*

1 Centre for Nanotechnology, Indian Institute of Technology-Guwahati, Assam 781039 India.
2 Department of Chemistry, Indian Institute of Technology-Guwahati, Assam, 781039 India,
3 William G. Lowrie Department of Chemical and Biomolecular Engineering, The Ohio State University, Columbus, OH, 43210, USA,
4 Department of Chemical Engineering, Indian Institute of Technology-Guwahati, Assam 781039 India.
5 Sustainability Institute, The Ohio State University, Columbus, OH, 43210, USA.
6 Jyoti and Bhupat Mehta School of Health Science & Technology, Indian Institute of Technology-Guwahati, Assam, 781039 India.

* Corresponding author: wang.12206@osu.edu and umanna@iitg.ac.in

Abstract:

Natural organisms often couple reversible shape reconfiguration and autonomous motion to adapt and respond to dynamic environments. However, synthetic soft materials rarely achieve both behaviors within a single platform due to fundamental trade-offs in structural anisotropy, solvent compatibility, and actuation reversibility. Here, we report a bicontinuous, uniaxially aligned liquid crystal elastomer-hydrogel composite (BALCEH) that allows both multi-stimuli shape reconfiguration and solvent-driven self-propulsion. The material integrates hydrophilic and hydrophobic networks, resulting in asymmetric solvent uptake and directional swelling across both aqueous and non-aqueous environments. This architecture supports reversible actuation under humidity, temperature, and organic solvents, governed by the interplay between anisotropic hydrogel expansion and LCE elasticity. BALCEH also achieves sustained Marangoni propulsion, with trajectory programmability through fuel composition and geometry. Additionally, spatial rearrangement of the dual networks imparts adaptive wettability, switching between superoleophobic and superhydrophobic states. By coupling deformation and motion in a single system, BALCEH offers a versatile platform for untethered soft robotics and intelligent, reconfigurable materials.

ARTICLE IN PRESS

Introduction

In nature, various plants, insects, and microorganisms exhibit two distinct modes of motion in response to external stimuli: a) reversible shape morphing without shifting its position (referred to as type I), and b) autonomous locomotion driven by interfacial forces (referred to as type II). The underlying principles for these two types of motion are fundamentally different. For example, type I motion includes the humidity-driven actuation of pinecone scales through asymmetric swelling[1,2] and rapid folding of seismonastic plant leaves in response to touch or vibrations[3]. In contrast, Rove beetles[4] (*Stenus comma*) secret a natural surfactant called stenusin[5] at the air/water interface, generating Marangoni force[6] to propel themselves, leading to type II motion. Additionally, certain bacteria, like *Caulobacter crescentus*, exhibit both type I and type II motions[7], where they alter their shape in response to perturbations in their surroundings and navigate using their flagella. Inspired by these natural systems, synthetic soft materials like liquid crystalline elastomers (LCEs)[8] and hydrogels have been designed to depict these two modes of motion. LCEs, which combine mesogenic anisotropy with the elasticity of polymers[9], demonstrate type I motion via phase transitions triggered by temperature, light, solvents, or electric fields[10]. However, LCEs are inherently unresponsive to water and incapable of propulsion (type II motion) due to their incompatibility with liquid environments and inability to release surface-active agents. Hydrogels, in contrast, are water compatible[11,12], but intrinsically lack the ability to undergo directional swelling and anisotropic shape changes[13]. Therefore, the integration of reversible, anisotropic shape morphing capable of enabling adaptive, asymmetric interactions and locomotion within a single soft material remains a significant design challenge.

To overcome this challenge, LCEs and hydrogels have been strategically modified to achieve hygroscopic LCE[14] and anisotropic hydrogels[13]. For example, the incorporation of hydrophilic polymers into cholesteric LCEs[15,16,17,18], post-synthetic treatment of LCEs in acidic[19,20] or alkaline conditions[21,22,23,24,25], and copolymerization of hydrophobic mesogens with photoactive and hydrophilic monomers[26,27,28,29] enabled modified LCEs for reversible hygroscopic actuation, humidity-gated photoactivation, and dual-responsive optical modulation. However, these systems still suffer from limited solvent uptake and lack interfacial propulsion action. Alternatively, incorporating various nanofillers, such as cellulose nanofibrils, fluorohectorite nanosheets, metal nanosheets, and graphene oxide, into hydrogel matrices through applying directional stimuli like shear forces[30], electric[31], and magnetic fields[32,33], or directed flow[34], yields composite anisotropic

ARTICLE IN PRESS

hydrogels. Additionally, the integration of metal nanoparticles[35] or high-aspect-ratio nanofillers[36] (e.g., modified graphene) enables self-assembly into anisotropic hydrogels. Furthermore, the association of oriented polymer chain networks[37,38], heterogeneous bilayer architecture[39,40,41], and top-down microfabrication techniques[42] can provide anisotropic hydrogels. However, prepared anisotropic hydrogels predominantly suffer from poor absorption of various non-aqueous solvents with low surface tension, which remains a primary requirement for achieving prolonged and fast type II motion. Very recently, Chen et al.[41] developed a bilayer actuator consists of a passive layer of elastomer and an active layer of glycol-based polymer gel. It exhibited a combination of deformation and propulsion depending on the glycol-water exchange process. Thus, its function is limited to a specific condition and remains inappropriate to modulate the motion trajectory.

Previously reported hydrogel- and LCE-based soft materials are generally associated with either type I or type II motions (Supplementary Table 1 and Supplementary Table 2), as the underlying mechanisms governing these two types of motions are fundamentally distinct. The designs of earlier systems typically focus on achieving one specific motion type, making the integration and interplay of both mechanisms particularly challenging. Here, we report a fundamentally different soft material, bicontinuous anisotropic LCE-hydrogel (BALCEH), having ability to exhibit both multi-stimuli–responsive type I and type II motions with customizable trajectories, through strategic integration of a uniaxially aligned LCE network within a porous, hydrophilic hydrogel scaffold. The resulting bicontinuous network of hydrophilic hydrogel and hydrophobic LCE allows asymmetric solvent absorption of both aqueous and non-aqueous solvents. The synergy between anisotropic swelling of the hydrogel and elastic restoring forces from the LCE leads to multi-stimuli shape transformation (type I), triggered by water, humidity, organic solvents, and temperature. Simultaneously, the BALCEH can retain and gradually release organic solvents (denoted as fuels), generating Marangoni-driven self-propulsion (type II) with customizable trajectories. The dynamic interplay of chemical functionality and structural anisotropy further enables adaptive liquid repellency, switching between superoleophobic and superhydrophobic states, depending on the immersion medium. By coupling shape programmability with solvent-responsive locomotion, this dual-mode actuation strategy in BALCEH provides a versatile platform for developing next-generation soft robotic systems, smart coatings, and bio-interfacing devices.

ARTICLE IN PRESS

Results

Preparation of bicontinuous anisotropic LCE-hydrogel (BALCEH) system

To achieve a soft material that combines anisotropic shape morphing and solvent-driven autonomous locomotion, we sought to design a composite system where a uniaxially aligned LCE network is embedded within a highly swellable, isotropic hydrogel matrix. A hydrogel scaffold was prepared by polymerizing the hydrophilic monomer N,N-dimethylacrylamide (DMA) with the crosslinker N,N'-methylenebis(acrylamide) (BIS) in an aqueous medium (see Experimental Section for details). The synthesized hydrogel was characterized using attenuated total reflectance-Fourier transform infrared spectroscopy (ATR-FTIR), where the successful polymerization of the selected acrylate monomers was confirmed by the disappearance of characteristic vinylic C–H peaks at 1418 cm^{-1} and 1410 cm^{-1} (Supplementary Fig.1).

The morphology of the freeze-dried hydrogel network was examined using field emission scanning electron microscopy (FESEM), confirming the existence of a highly porous structure (Supplementary Fig. 2). The high porosity and chemical functionality enable efficient swelling in both aqueous (swelling ratio of ~1100%) and various organic solvents (>120%) (Supplementary Fig. 3). Such solvent swelling is essential for the loading of LCE precursors, including reactive mesogen 1,4-bis-(4-(3-acryloyloxypropyloxy)benzoyloxy)-2-methylbenzene (RM257), non-mesogenic diacrylate spacer 1,6-hexanediol diacrylate (HDDA), crosslinker pentaerythritol tetrakis(3-mercaptopropionate) (PETMP), and a non-reactive mesogen 4-cyano-4’-pentylbiphenyl (5CB) (compositions for BALCEH is provided in Table 1).

To polymerize the LCE within the hydrogel scaffold, we adopted a two-step crosslinking approach. A partially crosslinked LCE was synthesized via a thiol-Michael addition reaction, as evident by ATR-FTIR analysis in Supplementary Fig. 4. Subsequently, tensile strain was applied to align the selected mesogen, followed by UV-induced crosslinking under the applied strain. This process resulted in a uniaxially aligned (monodomain) LCE network in the prepared BALCEH. A sufficiently high degree of crosslinking in the initial step is crucial to incur essential tensile deformation for the LCE mesogen alignment within the porous hydrogel scaffold. It is worth to mention that photopolymerization of residual acrylate moieties from RM257 and HDDA was conducted in the presence of nonreactive mesogen nematic 5CB[43]. The resulting BALCEH was characterized using ATR-FTIR (Fig. 1d). The infusion of precursors for LCE into the porous hydrogel scaffold resulted in the appearance of characteristic IR signals at 1410 cm^{-1} and 1726

ARTICLE IN PRESS

cm^{-1}, which correspond to vinylic C–H and carbonyl stretching, respectively[44] (Fig. 1d, orange line). After UV curing, the disappearance of the IR signal at 1410 cm^{-1} confirms the complete polymerization of the infused precursors, yielding a bicontinuous network of hydrogel and LCE (Fig. 1d, cyan line). Raman spectroscopy further validated the bicontinuous distribution of both networks. Spectra recorded at three arbitrary locations across the BALCEH cross-section (Fig. 1e) consistently showed peaks corresponding to both LCE [3080 cm^{-1} and 2933 cm^{-1} (C–H stretch), 1731 cm^{-1} (ester C=O), 870 cm^{-1} (C–S), and 1608 cm^{-1} (aromatic C=C)], and hydrogel [3080 cm^{-1} and 2933 cm^{-1} (C–H stretch), 3210 cm^{-1} (N–H stretch), and 1169 cm^{-1} (C–N)] components, confirming a uniform distribution of both networks[45].

Polarized optical microscopy (POM) provided evidence of uniaxial alignment within the LCE network. When the LCE director orientation was aligned either parallel or perpendicular to the polarizers, the sample exhibited no light transmission across the polarizers (Supplementary Fig. 5, and Fig. 1f). In contrast, the sample exhibited a bright appearance when its director orientation was altered, reaching the brightest signal at 45° relative to the polarizers (Fig. 1F), characteristic of uniaxially aligned mesogens[46]. BALCEH prepared without applied tensile strain exhibited non-uniform mesogen orientation and non-uniform brightness (Supplementary Fig. 6 and Fig. 1f), confirming that an applied unidirectional tensile strain contributes to aligning LC mesogens in the hydrogel scaffold, developing uniaxially aligned LCE. Thereafter, the orientation parameter (S) for BALCEH prepared with (~150%) and without uniaxial mechanical stretching during the photocuring step was experimentally determined using wide-angle X-ray scattering (WAXS, Fig. 1g–i and Supplementary Fig. 7). The 2D scattering image (Fig. 1g) for the uniaxially aligned BALCEH shows two high-intensity arc regions, indicating pronounced anisotropy. In contrast, samples prepared without any stretching exhibit a uniform diffraction ring, characteristic of isotropic or polydomain structures. Azimuthal intensity profiles in Fig. 1i were obtained by accounting the signal at 2Θ ~14°. The order parameter for the uniaxially stretched BALCEH (~150% strain) was determined to be S = 0.53, whereas the sample prepared without external tensile strain exhibited a much lower value of S = 0.17.

Additional field-emission scanning electron microscopy (FESEM) (Supplementary Fig. 8) and atomic force microscopy (AFM) (Supplementary Fig. 8) analysis showed distinct morphologies for BALCEH with uniaxially and randomly aligned LCE network. Uniaxially aligned BALCEH displayed a smoother surface, with a lower root mean square roughness (R_q ~28±2 nm) compared

ARTICLE IN PRESS

to its randomly aligned counterpart (R_q ~52±3 nm). Overall, these results confirm the successful fabrication of a bicontinuous composite comprising of an anisotropic, strain-aligned LCE network embedded within an isotropic, solvent-swelling hydrogel matrix.

Interfacial wetting transition and anisotropic mechanical properties of LCE-hydrogel (BALCEH)

With the bicontinuous structure of the BALCEH, we sought to investigate how the chemical and morphological properties of the hydrogel and LCE networks govern their adaptive, solvent-responsive interfacial behavior. Due to their distinct wettability characteristics (e.g., hydrophilic for the hydrogel network and hydrophobic for the LCE network), the prepared BALCEH displays contrasting surface wettability under immersion, depending on the surrounding solvent environment. In water, the hydrogel network displays extreme repellence for beaded droplets of model oil (e.g., dichloroethane) with a contact angle (CA) of ~154° (Fig. 2a, top), while exhibiting high affinity for beaded water droplets with CA of 0° when submerged under oil (Fig. 2a, bottom). In contrast, the LCE remains highly water-repellent under heptane (model oil phase) with a CA of ~153° (Fig. 2b, bottom), while oil droplet beads on this same surface underwater, displaying a low CA of ~24° (Fig. 2b, top). By tuning the relative weight ratio of LCE to hydrogel within the composite, we identified an optimal formulation at LCE: hydrogel = 1.5:1, which maximized repellency under both immersion conditions, exhibiting CA > 150° for both underwater superoleophobicity and underoil superhydrophobicity (Fig. 2c, d and Supplementary Fig. 9).

We hypothesized that these immersion-dependent wetting behaviors arise from solvent-selective surface expression and rearrangement of each network (Fig. 2e). To test this hypothesis, we conducted experiments to examine solvent-specific behavior. Firstly, the BALCEH appears translucent under water, due to partial swelling and light scattering from the hydrogel phase, whereas it becomes completely opaque in oil, indicating predominant LCE swelling (Fig. 2f). Secondly, Raman spectra of BALCEH equilibrated separately in water and heptane closely resemble those of water-swollen hydrogel and oil-swollen LCE, respectively (Fig. 2g), confirming solvent-driven compositional partitioning at the interface. Further, the Raman mapping based on the characteristic signatures at 1608 cm^{-1} (aromatic C=C stretching, LCE) and, 3210 cm^{-1} (N–H stretching, hydrogel) (Fig. 2h) shows that both signals are present in the dry state, whereas exposure to either water or a model oil phase causes the corresponding network-specific signal to dominate. This solvent-dependent spectral redistribution reveals a spatial rearrangement of the two

ARTICLE IN PRESS

interpenetrating networks during swelling, directly linking network reorganization (Schematically depicted in Fig. 2i) to the observed wettability switching. These results indicate that the interfacial chemistry of the BALCEH is dynamically reconfigurable, dictated by the external solvent environment[47]. This enables adaptive and reversible switching between extreme water and oil repellency, a feature unachievable with either network alone. Such adaptive and extreme liquid wettability offers significant potential in various applications, including the development of smart coatings via surface engineering[48], droplet manipulation[49], sensing[50], information encryption[51], and wetting-enabled microfluidic devices[52].

Complementing the surface behavior, the prepared BALCEH exhibited direction-dependent mechanical enhancement, comparable to pure LCE systems[8,10,53]. The hydrogel without the addition of the LCE displayed low, isotropic mechanical stiffness, with a Young's modulus of ~0.04±0.002 MPa, regardless of strain direction (Fig. 3a and Supplementary Fig. 10). In contrast, the LCE showed pronounced anisotropy, with Young's moduli of ~1.95±0.11 MPa and ~2.82±0.26 MPa when strained perpendicular and parallel to the LC director, respectively. The combination of LCE and hydrogel in BALCEH increased the Young's modulus to ~4.05±0.38 MPa and ~8.03±0.87 MPa in the perpendicular and parallel direction of applied tensile strain, respectively, more than doubling the LCE's mechanical stiffness in both directions. Mechanical anisotropy in liquid crystal elastomers (LCEs) arises from several interconnected factors, including the degree of orientational order, network heterogeneity introduced by non-mesogenic components, mesogen density, the magnitude of imposed uniaxial strain during mesogen alignment, director fluctuations at crosslinking points, and the measurement temperature[54,55,56,57]. In this work, the LCE network was prepared using the RM257, where a highly crosslinked chemistry is employed. This LCE network combined with non-mesogenic content likely contributes to the observed modest mechanical anisotropy response. A comparable order of mechanical anisotropy was also found in previous LCE studies[57,58,59]. Finally, our BALCEH system demonstrated excellent flexibility, withstanding common mechanical deformations like folding, twisting, and creasing (Fig. 3b), and is capable of supporting a static load of 100 g (500× its own weight, ~ 200 mg) without failure (Fig. 3c). The modulus of toughness for prepared BALCEH are ~449.9±28 kJ m^{-3} and ~1313.8±33 kJ m^{-3} in the parallel and perpendicular direction to the director, respectively, (Fig. 3a) confirming

its anisotropic fracture behaviour. While this, we found relatively poor toughness modulus for

ARTICLE IN PRESS

individual networks (either hydrogel or LCE). Thereafter, the cyclic loading performed at half of the fracture strain exhibited negligible hysteresis when tested over 20 cycles, demonstrating the durability and resilience of the bicontinuous BALCEH network (Supplementary Fig. 11). These findings confirm the importance of the hybrid architecture to not only preserve the anisotropic mechanical character of LCE but also enhance mechanical resilience through its continuous structure.

Stimuli-responsive reversible deformation of LCE-hydrogel (BALCEH)

Building on its adaptive interfacial and mechanical properties, we next investigated the ability of the BALCEH to undergo reversible, stimulus-responsive shape morphing. This functionality is essential for mimicking natural systems in which environmental changes drive cyclic structural transformations. We individually exposed arc-shaped strips of hydrogel and LCE to liquid water. Upon immersion in water, the hydrogel strip rapidly straightened within a minute (Fig. 4a) due to isotropic swelling. However, upon drying, the original curvature was not retained, confirming the deformation was irreversible. The LCE strip showed no response to water immersion (Fig. 4b), consistent with the water-inert nature of its hydrophobic mesogenic network. In contrast, the BALCEH displayed a reversible shape transformation under the same conditions. When immersed in water, the arc gradually relaxed, with its curvature decreasing from ~0.510±0.008 mm^{-1} to ~0.250±0.003 mm^{-1} over 5 minutes (Fig. 4c, d and Supplementary Movie 1). Upon removal and ambient drying, the strip regained its original shape (Fig. 4c, d and Supplementary Movie 2). The swelling of a polymeric hydrogel in water leads to a conformational rearrangement of polymer chains, and resulted in a decrease in Young's modulus (from ~0.04±0.002 MPa to ~0.019±0.003 MPa). In contrast, the LCE network remains largely insensitive to the aqueous environment, maintaining its mechanical integrity with an unaltered modulus (~2.82±0.26 MPa ∥ and ~1.95±0.11 MPa ⊥). We hypothesized that the reversible actuation of BALCEH arises from the interplay of two forces, i.e., anisotropic swelling of the hydrogel network and elastic restoring forces from the aligned LCE network. During water exposure of BALCEH, the swelling of the hydrogel network generates internal strain that drives shape deformation, whereas the hydrophobic LCE domains resist this expansion. Upon drying, the elastic restoring force of the LCE network facilitates the recovery of the original shape. In comparison, a pure hydrogel lacks this elastic counterforce and therefore fails to recover its initial geometry after dehydration. Time-dependent

ARTICLE IN PRESS

curvature analysis revealed linear deformation. The hydrogel exhibited the fastest underwater unfolding (8.2×10^{-3} $mm^{-1}s^{-1}$), about ten times higher than the BALCEH strip (8.5×10^{-4} $mm^{-1}s^{-1}$), while the LCE sample showed a constant curvature, indicating no response upon aqueous exposure, as shown in Fig. 4d. BALCEH, which exhibits a uniaxially oriented monodomain LCE, generates a directional elastic restoration force that allows reversible type I actuation. In contrast, the polydomain LCE counterpart fails to recover its shape under identical experimental conditions (Fig. 4d and Supplementary Fig. 12), as the random orientation of domains prevents the development of a net elastic restoring force during water evaporation. Together, these results indicate that the anisotropic, bicontinuous architecture of the hydrogel and LCE monodomain networks plays a synergistic role in enabling the reversible, water-induced shape transformation.

The Polarized optical microscopic (POM) study during water swelling showed that expansion occurred primarily orthogonal to the director (Fig. 4e and Supplementary Fig. 13), with a concurrent loss of birefringence (Fig. 4e and Supplementary Fig. 14), likely due to temporary and partial disruption of the mesogen ordering. Upon drying, birefringence reappeared (Fig. 4f and Supplementary Fig. 15), indicating the realignment of the LCE domains and recovery of the preprogrammed shape (Schematically depicted Fig. 4g). Notably, the expansion of BALCEH occurs predominantly perpendicular to the LC director due to the swelling of the embedded hydrogel network. However, a smaller degree of expansion along the director is also observed (Supplementary Fig. 14). Initially, the strip expands primarily perpendicular to the director, while expansion along the director becomes evident only after sufficient perturbation of mesogen alignment. To quantify swelling-induced perturbations in mesogen ordering, we analyzed the mean grayscale intensity of birefringence arising from the LCE monodomain under identical imaging conditions (Supplementary Fig. 16). The normalized intensity decreased to ~20% of its initial value within 15 min of water swelling and then reached a plateau. Upon ambient deswelling, the intensity recovered >99%, indicating complete restoration of mesogen ordering of LCE monodomain. The reversible type I motion by BALCEH is successfully repeated for at least 10 cycles, demonstrating the repeatability of the actuation mechanism with minimal degradation (Supplementary Fig. 17). Similar reversible responses were observed in other polar solvents such as ethanol (Supplementary Fig. 18).

To quantify actuation dynamics, we analyzed the shape evolution in solvents of varying polarity, which influences the degree of swelling of the hydrogel network (Supplementary Fig.

ARTICLE IN PRESS

19). We defined two parameters: *L*, representing the end-to-end distance of the bent strip, and α is the angle between *L* and the vertical axis to which the strip is attached (as depicted in Fig. 4c). As the strip extends, both *L* and α gradually increase over time. Our results indicate that the rate of increase in *L* accelerates with increasing solvent polarity (Supplementary Fig. 20), and a similar trend is observed for the evolution of α (Supplementary Fig. 20). As the BALCEH strip dries and water evaporates under ambient conditions, the material refolds, where the rate of solvent evaporation dictates the speed of refolding (Supplementary Fig. 21). It is worth to mention that the type I actuation of BALCEH slows with increasing thickness. Strips of ~296±4 µm, ~490±6 µm, and ~680±3 µm showed progressively longer actuation durations, while studied with similar initial curvature (Supplementary Fig. 22).

Reversible shape morphing of BALCEH was also observed under variable humidity. A coil-shaped BALCEH exposed to high relative humidity (RH ~98%) swelled and transformed into a closed loop due to water condensation. When returned to ambient humidity (RH ~45%), the structure relaxed back to its original shape (Fig. 4h), demonstrating humidity-induced deformation. Finally, the BALCEH showed thermally responsive contraction, a characteristic of LCE phase transition-induced shape change[24,60,61]. Heating to ~75 °C caused uniaxial shrinkage (~15%) along the director due to the transition to an isotropic mesogen state. Upon cooling, the material recovered its original length (Fig. 4i). Differential scanning calorimetry (DSC) confirmed the phase transition, showing an endothermic peak at 73 °C (Supplementary Fig. 23). These results confirm that the BALCEH exhibits reversible, multi-stimuli-responsive deformation, driven by coupled swelling-deswelling and mesogen reordering.

Solvent-fuelled autonomous motion with programmable trajectories

Inspired by the Marangoni-driven locomotion of Rove beetles (Fig. 5a), we investigate whether the prepared BALCEH can mimic such behavior, achieving type II motion. To achieve this behaviour for a prolonged duration, a soft actuator must satisfy two requirements: (1) buoyancy at the air–water interface, and (2) controlled release of low-surface-tension solvents. We found that our BALCEH possesses both criteria: it can float at the air–water interface and can absorb and retain a wide range of low surface-tension organic solvents (e.g., ethanol, acetonitrile (ACN), N,N-dimethylformamide (DMF), dimethyl sulfoxide (DMSO), dichloroethane (DCE), ethyl ether) (Supplementary Fig. 24). As a proof of concept, we loaded a rectangular BALCEH strip (5 mm ×

ARTICLE IN PRESS

2.5 mm × 1 mm) with ethanol and placed it on the surface of a water pool (9 cm diameter, 1.5 cm depth, 30 mL water), as depicted in Fig. 5b. The strip immediately exhibited autonomous circular motion at the air–water interface for approximately 26 minutes (Fig. 5c and Supplementary Movie 3). The same behavior was observed across various BALCEH geometries, including triangles, squares, and disks (Supplementary Fig. 25 and Supplementary Movie 3), suggesting that this motion is attributed to asymmetric ethanol diffusion (Supplementary Fig. 26). Generally, a local surface tension gradient on the water surface, arising from local variations in either the concentration of low-surface-tension substances or temperature, contributes to the Marangoni flow [6,62,63,64]. In our current study, the uniaxially aligned LCE phase in the prepared BALCEH induces anisotropic swelling, which leads to uneven diffusion of low–surface-tension liquids in the surrounding water pool. As a result, a local surface tension gradient develops around the BALCEH, driving its Marangoni propulsion on the water/air interface. We observed an immediate quenching of the self-propulsion of BALCEH when the local surface tension gradient on the water surface was disrupted by the external addition of ethanol (500 μL) during its motion, as demonstrated in Fig. 5d, Supplementary Fig. 27, and Supplementary Movie 4. Furthermore, we calculated the Marangoni number (M_a), which represents the ratio of surface tension effects to thermal effects, defined as (Eq. (1));

$$M_a = \Delta\gamma L'/\mu D \qquad (1)$$

where $\Delta\gamma$ is the surface tension difference between the solvent loaded in BALCEH and the surrounding water, μ, D, and L' denote liquid viscosity, diffusion coefficient, and the characteristic length ranging from the strip of BALCEH to the water pool. For ethanol-swollen BALCEH, we estimated a very high M_a of 8.9×10^{12}, indicating that the propulsion of BALCEH does not originate from thermal Marangoni flow. Subsequently, we examined the thermal environment using infrared (IR) thermography and detected no measurable temperature gradients around the self-propelling strip during motion in the water pool (Fig. 5e). These results collectively rule out the possibility of thermal-gradient-induced Marangoni flow as the driving mechanism for BALCEH propulsion. Rather, its propulsion is guided by the asymmetric release of low surface tension substance from BALCEH in the water pool. In contrast, a conventional hydrogel, although capable of absorbing 6× more ethanol, exhibited only a short-lived, random motion (~5 min, Fig. 5c and Supplementary

ARTICLE IN PRESS

Fig. 28). A key difference between BALCEH and a conventional hydrogel lies in their different water absorption capacities. The swelling ratios of the hydrogel and BALCEH are ~1100% (Supplementary Fig. 19) and ~315% (Supplementary Fig. 24), respectively. Owing to its high water compatibility, the hydrogel becomes fully immersed after water absorption, remaining suspended beneath the air–water interface and readily adhering to the walls of the water reservoir (Supplementary Fig. 29), which suppresses autonomous motion. In contrast, BALCEH consists of a bicontinuous network composed of a hydrophobic, uniaxially aligned LCE monodomain and a hydrogel phase. This architectural design limits overall water uptake and makes BALCEH remain stably floating at the air–water surface for prolonged durations. Moreover, the presence of LCE monodomain induces anisotropic swelling of BALCEH even in ethanol (Supplementary Fig. 26). This anisotropic swelling leads to direction-dependent diffusion and release of ethanol at the air–water surface, thereby generating surface tension gradients. As a result, stable flotation, high ethanol loading capacity, and anisotropic solvent diffusion result in sustained type II actuation observed in BALCEH. Thus, sustained Marangoni propulsion requires both floatation at the air–water interface and the maintenance of a surface-tension gradient over time. Ethanol-swelled hydrogels fail in this regard due to rapid, isotropic water ingress and subsequent loss of buoyancy. In contrast, the bicontinuous BALCEH architecture, featuring a hydrophobic and anisotropic LCE phase, ensures stable floatation and a prolonged surface-tension gradient, enabling continuous Marangoni-driven motion. LCEs alone, by comparison, absorbed <2 wt.% ethanol and showed no motion (Fig. 5c and Supplementary Fig. 30). In addition, the type II motion of BALCEH is influenced by sample dimensions. Larger area or thickness increases propulsion time, likely because greater volume retains more solvent, sustaining the surface tension gradient required for prolonged type II motion (Supplementary Fig. 31).

It is also noteworthy that the shape and dimensions of the water pool influence the trajectory of the moving BALCEH. For example, when the experiment was conducted in a square-shaped container (side length: 10 cm), the BALCEH adopted a square trajectory (Supplementary Fig. 32). Even, it travels along a straight-line path across the water surface, as demonstrated in Supplementary Fig. 33. These experiments demonstrate that cooperative coupling between the anisotropic LCE and the swelling hydrogel networks is critical for sustained, directional self-propulsion.

Next, we explored how the choice of solvent fuel (varying in water miscibility and volatility)

ARTICLE IN PRESS

affects the self-propulsion behavior (Fig. 5f). Solvents that were water-miscible and volatile (e.g., ethanol, acetonitrile) produced the longest-duration motion, as they readily formed solutocapillary gradients via both diffusion into water and evaporation into air[65,66,67] (Fig. 5f and Supplementary Fig. 34). In contrast, non-volatile fuels (e.g., DMF, DMSO) showed reduced propulsion efficiency, and water-immiscible non-volatile fuels (e.g., decane, dodecane) yielded no motion (Supplementary Fig. 35). Volatile but water-insoluble fuels (e.g., DCE, ethyl ether) produced short-lived propulsion due to interfacial tension gradients induced via evaporation asymmetry[64] (Supplementary Fig. 36). These results demonstrate how fuel miscibility and volatility affect propulsion lifetime and efficiency. Such shape-independent propulsion from a broad fuel library is rare in previously reported soft actuators (Supplementary Table 3), further highlighting the versatility of the BALCEH. Thereafter, the self-propulsion of BALCEH can be dynamically modulated by externally perturbing the local surface tension gradient. Addition of a volatile, water-immiscible solvent temporarily quenches motion by disrupting the Marangoni force, which is fully restored upon solvent evaporation, allowing the object to resume its original trajectory (Fig. 5g, Supplementary Fig. 37, and Supplementary Movie 5).

Thereafter, building on these features of the BALCEH, we explored the combination of two different fuels to be used to drive external objects and program trajectory profiles. First, an ethanol-loaded BALCEH was attached to a 3D-printed triangular object (8× heavier than the actuator). Upon placement in water, the assembly underwent sustained circular motion for ~10 minutes (Fig. 6a; Supplementary Movie 6). When a three-armed star-shaped object was equipped with three ethanol-loaded BALCEH strips, it underwent simultaneous rotation and revolution (Supplementary Movie 7), driven by torque imbalance and continuous solvent release. To further program the motion trajectory, we attached two BALCEH strips loaded with different fuels (ethanol and DCE, with the DCE dyed with Nile red for visualization) to a 3D-printed triangular object (Fig. 6b). The resulting object initially moved in a circular path (Fig. 6b), followed by a transition into rotary motion once the faster-evaporating DCE had depleted (Supplementary Movie 8). This change in trajectory arises from asymmetric force evolution, as visualized in Fig. 6c: initially, both forces align with the centre of mass (Fig. 6c(i)); after partial DCE depletion, imbalance develops (Fig. 6c(ii)); once torque exceeds a threshold, rotary behavior emerges (Fig. 6c(iii)). Control experiments using symmetric fuel loading (e.g., ethanol–ethanol) only produced stable circular trajectories (Supplementary Fig. 38). Combining this concept with externally added

ARTICLE IN PRESS

immiscible solvent assisted temporarily quenching type II motion, we depicted a triggered switching of motion trajectory. A 3D printed object embedded with two BALCEH strips soaked in ethanol and DCE initially propels along a circular path, but temporary solvent addition halts motion. As evaporation restores the surface tension gradient, asymmetric force evolution drives the object along a rotational trajectory (Fig. 6d, Supplementary Fig. 39, and supplementary Movie 9), demonstrating programmable, stimulus-responsive control of soft robotic motion.

Next, we strategically designed a time-evolving trajectory system by combining propulsion and shape-morphing behaviors. Two ethanol-loaded BALCEH strips were paired with a bent, dry BALCEH actuator affixed as a navigation tail. As the structure absorbed water and slowly expanded, the radius of its circular trajectory increased, inducing a vortex-like outward spiral motion (Fig. 6e–g and Supplementary Movie 10). These findings establish design principles for exploiting inter-network coupling between actuation and morphing to encode dynamic motion pathways in soft robotic systems.

Finally, we employed the BALCEH strip as a solvent-responsive transport module enabling gated chemical reactivity in a multi-liquid system. Owing to its selective response to water, the BALCEH-based prototype (Supplementary Fig. 40, and Supplementary Movie 11) having three arms unfolds only upon aqueous exposure, remaining mechanically inert in non-polar hydrocarbons. The prepared actuator successfully and spatially selectively transported required reactants through a biphasic system to perform Schiff base reaction with two different set of reactants. On the other side, we established a gravity-driven strategy for the simultaneous separation and collection of oil and water by exploiting the adaptive and extreme liquid-wettability of BALCEH (i.e., underwater superoleophobicity and underoil superhydrophobicity). A porous polyurethane fabric, which intrinsically exhibits strong affinity toward water and oil under their respective submerged conditions, was selected as the support substrate. BALCEH deposition (4 mg cm^{-2}) endowed the fabric with adaptive and extreme wettability responses in both environments (Supplementary Fig. 41a, b). To evaluate separation performance, we developed a laboratory-scale prototype in which BALCEH-coated fabrics were mounted at the two ends of a hollow glass tube (Supplementary Fig. 41c). Prior to introducing the oil/water mixture through the central inlet, the left and right BALCEH-coated fabrics were equilibrated with oil and water, respectively. The complementary underwater superoleophobic and under-oil superhydrophobic states selectively permitted the passage of water and oil through opposite ends of the device, enabling efficient,

ARTICLE IN PRESS

gravity-driven phase separation and collection (Supplementary Fig. 41d, Supplementary Movie 12). Thus, prepared material can be potentially extended as soft robotic actuators to perform programmed chemical reactions, energy-efficient environmental remediation, etc.

Discussion

We have developed BALCEH, a multifunctional soft material that integrates programmable deformation, autonomous motion, and adaptive wettability by combining uniaxially aligned LCEs with a porous hydrogel scaffold. This bicontinuous network design allows rapid, anisotropic swelling and elastic recovery across a wide range of solvents and stimuli, supporting reversible shape transformations that are inaccessible to conventional hydrogels or LCEs alone. Importantly, the BALCEH exhibits sustained Marangoni-driven propulsion, regardless of shape symmetry, powered by directional release of volatile fuels, with high efficiency and controllable trajectories. The system further allows dynamic liquid repellency through solvent-mediated network rearrangement, offering switchable superoleophobic and superhydrophobic behaviors. By coupling responsive deformation with directional motion in a single material system, this platform opens opportunities for untethered soft robotics, intelligent floating devices, and adaptive surface engineering in aqueous environments.

ARTICLE IN PRESS

Methods

Materials: N,N-dimethylacrylamide (DMA; molecular weight: 99.13 g mol^{-1}; purity: 99%; CAUTION: causes acute oral and dermal toxicity), N,N'-methylenebis(acrylamide) (BIS; molecular weight: 154.17 g mol^{-1}; purity: 99%; CAUTION: causes skin and eye irritation), ammonium persulfate (APS; molecular weight: 228.20 g mol^{-1}; purity: ≥98%), 1,6-hexanediol diacrylate (HDDA; molecular weight: 226.27 g mol^{-1}; purity: >80%), pentaerythritol tetrakis(3-mercaptopropionate) (PETMP; molecular weight: 488.66 g mol^{-1}; purity: >95%; CAUTION: strong odour and causes allergic skin irritation), triethylamine (TEA; molecular weight: 101.19 g mol^{-1}; purity: ≥99.5%; CAUTION: strong odour and causes allergic skin irritation), aniline (molecular weight: 93.13 g mol^{-1}; purity: ≥99.5%; CAUTION: highly hazardous), decylamine (molecular weight: 157.30 g mol^{-1}; purity: 95%), vanillin (molecular weight: 152.15 g mol^{-1}; purity: 99%), methylene blue (purity: ≥82%), Nile red (purity: ≥97%) were purchased from Sigma-

ARTICLE IN PRESS

Aldrich (Bangalore, India). 2-hydroxy-2-methylpropiophenone (HMP; molecular weight: 164.20 g mol^{-1}; purity: >96%) was purchased from Tokyo Chemical Industry (India) Pvt. Ltd. Diacrylate mesogen 1,4-bis-(4-(3-acryloyloxypropyloxy)benzoyloxy)-2-methylbenzene (RM257; molecular weight: 588.60 g mol^{-1}; purity: >97%), non-reactive mesogen 4-cyano-4'-pentylbiphenyl (5CB; molecular weight: 249.35 g mol^{-1}; purity: 99.9%) were purchased from Kindchem Co. Ltd, China. Ethanol was procured from Changshu Hongsheng Fine Chemical. Acetone, tetrahydrofuran (THF), toluene, 1,2-dichloroethane (DCE), hexane, heptane, ethyl ether, N,N-dimethyl formamide (DMF), and acetonitrile (ACN) were purchased from Finar, India. De-ionized (DI) water was used for all the experiments. All reagents were analytical reagents and used as received without any further purification.

Characterizations: All the contact angles were recorded using the KRUSS Drop Shape Analyzer-DSA 25E instrument, and the measurements were performed with 5 µL de-ionized water/ oil (DCE as model) droplets at three different positions of each sample. A Carl Zeiss field emission scanning electron microscope (FESEM) was used to analyze the surface morphology of the freeze-dried hydrogel and bicontinuous LCE-hydrogel (BALCEH) samples. Before imaging, the samples were sputtered with a thin gold layer for 120 s. A LABCONCO 4.5 lyophilizer was used to freeze-dry the prepared samples. Atomic force microscope (AFM) images of freeze-dried samples were obtained using the OXFORD Cypher Atomic Force Microscope at ambient conditions. A PerkinElmer UTAR Two instrument was used to record attenuated total reflectance-Fourier transform infrared (ATR-FTIR) spectra, and the measurements were performed in ambient conditions. Zwick Roell (model: Z005TN Proline) electro-mechanical Universal Testing Machine (UTM) was used to monitor the tensile stress-strain relation. The cyclic loading performance was monitored using Instron-5944 Bio-plus UTM instrument. Thermal infrared (IR) camera (Testo-05608721) was used to perform IR-thermography. The phase transition temperatures were measured using a Mettler Toledo DSC1 differential scanning calorimeter instrument under a nitrogen atmosphere. Bright-field and polarized light optical microscopic (POM) images of prepared samples were captured using the 3 Zeiss Axio Vert-A1 inverted microscope equipped with a polarizer and an analyzer. Raman spectra were recorded using a LabRam HR800 Jobin Yvon spectrometer with an excitation wavelength of 532 nm (Ar ion laser). Wide-angle X-ray scattering (WAXS) experiment were performed in transmission mode using a Xenocs XEUSS

ARTICLE IN PRESS

SAXS/WAXS system equipped with a Genix microfocus source operating at 50 kV and 0.6 mA. The Cu Kα radiation (λ = 1.54 Å) was collimated with two pairs of scatterless slits and a FOX2D mirror. A Samsung Galaxy A51 SM-A516N cell phone camera was used to record all the videos. All the digital images were taken using a Nikon Coolpix B700 digital camera.

Preparation of the hydrogel: Hydrophilic monomer N,N-dimethylacrylamide (DMA) and crosslinker N,N′- methylenebis(acrylamide) (BIS) were used to prepare a hydrogel network following the thermally activated radical polymerization method in water, where ammonium persulfate (APS) was utilized as a radical initiator. The pre-gel solution was prepared by dissolving DMA (2.42 mmol, 240 mg), BIS (15.5 µmol, 2.4 mg), and APS initiator (13 µmol, 3 mg) into 1 mL of DI water. The prepared solution was agitated well for 10 minutes for homogeneous mixing and transferred into the desired moulds, then kept in a hot air oven at 75 °C for ~2 h. The synthesized hydrogel was removed from the mould and washed thoroughly with water prior to its freeze-drying.

Preparation of LCE: Monodomain LCE was prepared following the conventional two-step strain-induced alignment method[68,69,70,71,72].

Step 1: Covalent crosslinking

To prepare the LCE precursor solution, the diacrylate mesogen RM257 (0.17 mmol, 100 mg) and non-mesogenic diacrylate HDDA (25.5 µmol, 5.8 mg) were taken in a glass vial, and the measured volume of toluene (50 µL) was added to it. It was then heated to 80 °C for homogeneous mixing. After cooling it down to room temperature, the UV photoinitiator HMP (30.4 µmol, 5 mg) was added to it, followed by the addition of PETMP (24 µmol, 11.8 mg) and the catalyst TEA (20 µmol, 2 mg). The solution was mixed well and then placed inside a vacuum chamber for few minutes to remove any air bubbles caused by the mixing process. Afterward, the solution was immediately poured into the desired mould and cured overnight to ensure complete 1,4-conjugate addition reaction between thiol and acrylate groups in the reaction mixture.

Step 2: UV photopolymerization under uniaxial mechanical strain

ARTICLE IN PRESS

After the covalent crosslinking step, the sample became visually opaque. The free-standing soft strip was then removed from the mould, and it was uniaxially stretched (~150% in length) and placed under a UV chamber for an hour to get the monodomain LCE with a uniform alignment of the mesogens.

Preparation of the BALCEH samples:

Three major steps were followed to prepare the BALCEH–

1. Infusion of LCE precursors into the hydrogel scaffold via swelling

To infuse the LC monomer (RM257) and non-mesogenic spacer (HDDA) in the hydrogel scaffold, a solution of LCE precursors was prepared in a solvent mixture of ethanol and acetone (1:2 volume ratio). The required amounts of RM257 and HDDA were utilized, are summarized in Table 1. To ensure complete infusion via swelling, the volume of the solvent mixture used to dissolve the LCE precursors was kept below the maximum solvent holding capacity of the respective hydrogel. Typically, a dried hydrogel strip was immersed in the prepared solution of LCE precursors and allowed to swell for approximately 12 h, with the vial securely capped. After complete infusion of the reaction mixture into the hydrogel, the swelled hydrogel strip was allowed to air dry. Following the evaporation of selected solvents, the appearance of the material transitioned from transparent to an opaque white.

2. Covalent crosslinking of the infused precursors via thiol Michael addition reaction

The loaded LCE precursor was then subjected to covalent crosslinking via thiol Michael addition reaction. This process involved the chemical reaction between the available acrylate groups and the added thiol. To prepare the crosslinker solution, precise amounts of each component (PETMP, HMP, TEA, 5CB) were taken according to Table 1 and dissolved in a predetermined volume of the solvent mixture (ethanol and acetone; 1:2 volume ratio). The total volume of the solvent was carefully chosen to ensure complete soaking of the prepared solution into the precursor-loaded hydrogel. Swelling-induced diffusion of the PETMP-containing solution into the precursors-loaded hydrogel scaffold facilitated the thiol Michael addition reaction. A visual transition from opaque white to transparent signalled the complete penetration of the crosslinker solution into the hydrogel scaffold.

ARTICLE IN PRESS

3. UV polymerization of reactive LCE monomer under uniaxial mechanical strain

The volatile solvents are allowed to evaporate, and the transparent strip turns opaque white again. The strip was then subjected to UV polymerization (365 nm) while being uniaxially stretched to ~150% of its original length for one hour to get the uniaxially aligned BALCEH. Photopolymerization without any stretching produced the non-aligned BALCEH. Finally, the soaked 5CB was removed by ethanol washing, followed by drying under vacuum to get the BALCEH. Here, 5CB does not participate in the polymerization but prevents the hydrogel network from becoming stiff and assists the strain-induced mesogen alignment.

Preparation of arc and helix-shaped BALCEH: After covalent crosslinking (step-2), the 5CB soaked strip was uniaxially stretched (~150 % in length), and the two ends were fixed around a glass tube with glue. Then, it was allowed for UV polymerization (365 nm) for an hour. To get the free-standing bent-shaped actuator, the attached ends were cut with a knife, washed with ethanol to remove the 5CB, and dried under vacuum. To get the helix-shaped BALCEH, both ends of the uniaxially stretched strip were wrapped around a glass tube as a support, in a helicoidal manner, and placed under UV (365 nm) for an hour; thereafter, the aforementioned method was followed to get the freestanding helix.

ARTICLE IN PRESS

Estimation of the swelling ratio: The swelling ratio (%) of the prepared materials in polar and nonpolar solvents was quantified following a widely accepted procedure[73,74,75]. The prepared samples were weighed after drying and immersed in test solvents. After ~24 h, samples were removed from the solvent, gently blotted with lint-free tissue paper to remove excess solvent on the surface, and weighed. The swelling ratio (%) was then calculated by the following equation (Eq. (2)):

$$\text{Swelling ratio (\%)} = (w_2 - w_1)/w_1 \times 100\% \quad (2)$$

where w_1 and w_2 represent the initial (dry) and final mass (swelled) of the samples, respectively. For each solvent, three different measurements were performed, and the average value is provided.

ARTICLE IN PRESS

Raman spectroscopic characterization of BALCEH: The prepared BALCEH samples (14 mm×6 mm×1.5 mm) were immersed in selected solvents (i.e., water or heptane). Fully swelled samples were taken out of the solvents, blotted with lint-free tissue paper to remove excess solvent on the surface, then it was placed on a glass slide and allowed to record Raman spectra immediately with an excitation wavelength of 532 nm (green LASER), objective of ×50 LWD, grating of 1800 gr/mm and ND filter.

Wide-angle X-ray scattering (WAXS) analysis: The orientation parameter (S) for uniaxially aligned BALCEH and its analogous sample prepared in absence of applied external tensile strain was experimentally determined using wide-angle X-ray scattering (WAXS). Fiber diffraction patterns were collected on a Mar345 image plate and processed using Fit2D. Silver behenate served as calibration standards for the WAXS. The image plate detector was positioned along the beam path at 217.8 mm from the sample for WAXS measurement. Measurements were performed at room temperature (22 °C), with samples directly mounted on the holder. Azimuthal intensity profiles were obtained by considering the signal at 2Θ ~14°. The 2D scattering image shows two high-intensity arc regions for uniaxially aligned BALCEH, an indication of anisotropy, whereas its analogous sample exhibits a uniform diffraction ring, denoting the existence of LCE polydomain. The orientation parameter (S) is calculated using following equation[76] (Eq. (3)).

$$S = (180° - \Delta\phi)/180° \quad (3)$$

where $\Delta\phi$ represents the full width at half maximum intensity.

Mechanical property of BALCEH: Rectangular-shaped thin BALCEH (35 mm×5 mm×0.5 mm) samples were utilized for tensile strength measurement using a pincer grip of a 5 kN electromechanical universal testing machine Zwick Roell (model: Z005TN). At the time of measurement, hydrogel and BALCEH samples contained ~10 wt.% of absorbed ambient moisture. The tensile stress was calculated by dividing the measured force by the cross-sectional area of the sample. Young's modulus was calculated from the slope of the stress versus strain relation. Modulus of toughness was calculated considering the total area under respective stress versus strain curve and reported in the unit of kJ m^{-3}.

Adaptive liquid wettability of BALCEH: A rectangular BALCEH strip (1.4 cm×6 mm×1.5 mm) was cut into two pieces and dried well. One of them was submerged in water (24 h) for its swelling,

ARTICLE IN PRESS

and oil (DCE) contact angles under water were measured with a 5 µL oil droplet at three different positions to get the average contact angle value and standard deviation. Similarly, another strip was kept under heptane and allowed to swell (24 h). Thereafter, water contact angles were measured under heptane following the aforementioned method.

Solvent-induced actuation: The prepared arc-shaped BALCEH strip (8 mm×1.5mm×0.5mm, principal curvature ~0.5 mm^{-1}) was dried well; one end of it was attached to a glass capillary with glue and immersed completely under selected solvents in such a way that there would be no air bubble attached to the sample surface. A square-shaped glass beaker was used as a solvent container, and a camera was placed in front of it to record the entire actuation process. The experiments were performed in ambient conditions. After completion of the unfurling process, the capillary with the attached swelled sample was taken out of the test solvent and kept under ambient conditions (temperature: 22 °C, relative humidity (RH) ~45%) for drying, and the shape-restoration process was recorded.

Humidity-induced actuation: A closed chamber with an outlet was taken, and a digital humidity sensor and a digital temperature sensor were attached inside the chamber to monitor its temperature and humidity. Then, the chamber outlet was connected to a commercially available mist-generating humidifier with a tube to get the water mist to flow inside the chamber for a long time. The helix-shaped BALCEH strip was dried properly, and one end was attached to a glass capillary with glue and placed inside the chamber in a hanging condition before the experiment. The relative humidity (RH) inside the chamber gradually increased over the period of time, and the helix-shaped BALCEH strip slowly unfurled to give a loop shape. The glass capillary with the sample was removed from the chamber and placed under ambient conditions to get back the helix shape after water evaporation.

Temperature-induced actuation: A rectangular, straight, thin uniaxially aligned BALCEH strip (26 mm×2.5 mm×0.3 mm) was thoroughly dried and then kept in ambient conditions (temperature: 22 °C, RH ~45%) before its exposure to elevated temperature (~75°C). Upon contact with the hot plate, the sample began to shrink along its long axis (the director axis). The sample was quickly removed from the hot plate as soon as possible and allowed to cool to ambient temperature.

ARTICLE IN PRESS

Marangoni motion with solvent-soaked BALCEH strip: A water pool was prepared by taking 30 mL of DI water in a glass petri dish (diameter: 9 cm, depth: 1.5 cm). Marangoni motion of the solvent-soaked BALCEH samples was performed on this water pool kept on a perfectly flat, vibration-free table. A camera was placed at the top of this setup to record the video of the entire motion. A completely swelled rectangular strip (5 mm×2.5 mm×1.2 mm) of BALCEH was removed from the test solvents and gently blotted with lint-free tissue paper to remove excess solvent from the surface. Then, it was placed on top of the water pool with a clean tweezer. The water of the pool was changed before every individual measurement. The same experiment was performed with three other shapes for the BALCEH strip, including a square shape (length: 3.1 mm, thickness: 1.2 mm), a disk shape (diameter: 3.5 mm, thickness: 1.2 mm), and a triangular shape (length of side: 4.7 mm, thickness: 1.2 mm) under similar experimental conditions. The control experiment with a hydrogel and LCE strip soaked with ethanol was performed under similar experimental conditions as mentioned above.

Propulsion of 3D printed swimmer: A filament-based 3D printer, Ultimaker-3, was used to fabricate the swimmer body using AA-0.4 print core. A computer-aided design of the swimmer's body was made using Fusion 360 software. The exported STL file was uploaded to the 3D printer for printing with a layer thickness of 100 µm. All the printed objects have a thickness of 0.8 mm. We chose polylactic acid (PLA) as a printing material due to its stability towards water and common organic solvents, as well as its lightweight and strength. Thereafter, a solvent-swelled BALCEH strips were attached to the 3D printed swimmer object in the proper position with commercially available glue, then gently blotted with lint-free tissue paper and immediately placed in the water pool to monitor the autonomous locomotion.

Generation of Marangoni motion profile: The Marangoni motion profiles were extracted from the recorded video files with the help of Tracker, a freely available video analysis and modelling software tool built on open-source Physics (OSP) Java framework. Prior to tracking, the videos were calibrated with respect to a scale in the software and a Cartesian coordinate system, taking the centre of the petri dish as the origin of the system. The scale was taken on the basis of the diameter of the Petri dish. The moving object was tracked with the help of an auto tracker, a

ARTICLE IN PRESS

function available in the software, which generates information on position with respect to time. The data obtained has the *x* and *y* components of the position and the *z* component as time.

Gated chemical reaction: We employed the BALCEH strip as a solvent-responsive transport module enabling gated chemical reaction in a multi-liquid system. To transport and followed by triggered delivery of selected reactant, i.e., vanillin, a lab-based prototype was fabricated, where three arc-shaped BALCEH strips were attached to a glass capillary. Next, the vanillin bead was prepared by melting crystalline vanillin (98.6 µmol, 15 mg) at ~85 °C, drop-casting the melt onto a glass slide, and allowing it to solidify upon cooling. The prepared prototype can easily hold this bead, followed by transport and delivery at the desired location. To depict its ability for a gated chemical reaction, a clean glass vessel was half-filled with water. Two small cylindrical cuvettes were submerged, where one contained an aniline solution (98.7 µmol, 9.2 mg in 4 mL DCE; L-1) and the other contained a decylamine solution (99 µmol, 15.6 mg in 4 mL DCE; L-2). Thereafter, heptane was placed on top of the aqueous phase to form a biphasic system. The entire experimental setup is kept in ambient conditions. Initially, we dropped the prepared vanillin bead onto this experimental set-up, it initially travelled through the heptane phase and was found to be confined at the heptane/water interface. Eventually, it failed to react with reactants placed under water. In contrary, the BALCEH actuator successfully and spatio-selectively transported the bead through the aqueous phase. Owing to its selective response to water, the BALCEH-based carrier, having three arms, unfolds only upon aqueous exposure, remaining mechanically inert in non-polar hydrocarbons. Using this property, we established a biphasic heptane–water platform in which DCE-containing reaction vessels were embedded within the aqueous layer. Water-triggered swelling induced controlled deformation, permitting programmed release of the bead above predefined reaction vessels (L-1 or L-2). Its placement in the aqueous phase right above L-1 (containing aniline in DCE) yielded a particular Schiff base, whereas its placement above L-2 (containing decylamine in DCE) produced another. These experiments show that reaction initiation requires concurrent satisfaction of two conditions: (i) solvent-selective actuation of the BALCEH strip and (ii) spatially resolved placement of the reactant carrier within the aqueous layer. The platform thus operates via AND-gate logic, enabling precise, conditionally gated chemical transformations.

ARTICLE IN PRESS

Gravity-driven separation of oil/water with a BALCEH-coated fabric:

Adaptive and extreme liquid-wettability (i.e., underwater superoleophobicity and under-oil superhydrophobicity) of BALCEH is strategically applied to demonstrate a gravity-driven simultaneous separation and collection of oil and water. A porous polyurethane fabric, which intrinsically exhibits strong affinity toward water and oil under their respective submerged conditions, was selected as the support substrate. In this relevance, two stretchable polyurethane fabrics (10×10 cm^2 each) were first spray-coated with the hydrogel precursor. After washing and drying, the fabrics were soaked in the LCE precursor solution. Following adequate drying, they were treated with PETMP solution. UV polymerization was carried out under an applied tensile strain of ~120%. A mass ratio of 1:1.5 (hydrogel: LCE) was maintained for the deposited coating. Thereafter, a laboratory-scale prototype was constructed by mounting the BALCEH-coated fabrics at both ends of a hollow glass tube. Prior to introducing the oil/water mixture through the central inlet, the left and right BALCEH-coated fabrics were equilibrated with oil and water, respectively. Nonpolar hydrocarbon solvent heptane (coloured with Nile red) and water (coloured with Methylene blue) were taken as representative oil and water for the demonstration.

Data Availability

The data that support the findings of this study are included within the Article and its Supplementary Information. Raw data can be obtained from the corresponding author upon request. Source data are provided with this paper as a source data file.

References:

1. Dawson, C., Vincent, J. F. V. & Rocca, A.-M. How pine cones open. *Nature* **390**, 668-668 (1997).

2. Eger, C. J. et al. The structural and mechanical basis for passive-hydraulic pine cone actuation. *Adv. Sci.* **9**, 2200458 (2022).

3. Guo, Q. et al. Fast nastic motion of plants and bioinspired structures. *J. R. Soc. Interface* **12**, 20150598 (2015).

4. Ke, X., Yong, H., Xu, F., Ding, H. & Wu, Z. Stenus-inspired, swift, and agile untethered insect-scale soft propulsors. *Nat. Commun.* **15**, 1491 (2024).

5. Dietz, A. A., Hofmann, M. J. & Motschmann, H. The role of surface viscosity in the escape

ARTICLE IN PRESS

mechanism of the Stenus beetle. *J. Phys. Chem. B* **120**, 7143-7147 (2016).

6. Scriven, L., Sterling, C. The Marangoni Effects. *Nature* **187**, 186–188 (1960).

7. P. Alexandre *et. al.* The Mechanical World of Bacteria. Cell **161**, 5, 988-997 (2015).

8. Herbert, K. M. et al. Synthesis and alignment of liquid crystalline elastomers. *Nat. Rev. Mater.* **7**, 23-38 (2022).

9. Nie, Z. Z., Wang, M. & Yang, H. Structure-induced Intelligence of Liquid Crystal Elastomers. *Chem. Eur. J.* **29**, e202301027 (2023).

10. Jiang, Z.-C., Liu, Q., Xiao, Y.-Y. & Zhao, Y. Liquid crystal elastomers for actuation: A perspective on structure-property-function relation. *Prog. Polym. Sci.* **153**, 101829 (2024).

11. Lim, D. Hydrophilic gels for biological use. *Nature* **185**, 4706 (1960).

12. Buwalda, S. J. et al. Hydrogels in a historical perspective: From simple networks to smart materials. *J. Controlled Release* **190**, 254-273 (2014).

13. Sano, K., Ishida, Y. & Aida, T. Synthesis of anisotropic hydrogels and their applications. *Angew. Chem. Int. Ed.* **57**, 2532-2543 (2018).

14. Pinchin, N. P. et al. Liquid Crystal Networks Meet Water: It's Complicated! *Adv. Mater.* **36**, 2303740 (2024).

15. Stumpel, J. E. *et al.* Stimuli-responsive materials based on interpenetrating polymer liquid crystal hydrogels. *Adv. Funct. Mater.* **25**, 3314-3320 (2015).

16. Deng, Z., Zhou, G. & de Haan, L. T. Preparation of an interpenetrating network of a poly (ampholyte) and a cholesteric polymer and investigation of its hydrochromic properties. *ACS Appl. Mater. Interfaces* **11**, 36044-36051 (2019).

17. Shi, X. *et al.* Wearable optical sensing of strain and humidity: a patterned dual-responsive semi-interpenetrating network of a cholesteric main-chain polymer and a poly (ampholyte). *Adv. Funct. Mater.* **31**, 2104641 (2021)

18. Zhang, L. *et al.* Preparation and properties of water-responsive films with color controllable based on liquid crystal and poly (ethylene glycol) interpenetrating polymer network. *Liquid Crystals* **49**, 1411-1419 (2022).

19. Kim, K. *et al.* 4D printing of hygroscopic liquid crystal elastomer actuators. *Small* **17**, 2100910 (2021).

20. Xu, L., Zhang, S., Yin, L. & Zhao, Y. Humidity-Sensing and Moisture-Steering Liquid Crystal Elastomer Actuator. *Small* **21**, 2412547 (2025).

ARTICLE IN PRESS

21. Harris, K. D., Bastiaansen, C. W. M., Lub, J. & Broer, D. J. Self-assembled polymer films for controlled agent-driven motion. *Nano Lett.* **5**, 1857-1860 (2005).

22. De Haan, L. T., Verjans, J. M. N., Broer, D. J., Bastiaansen, C. W. M. & Schenning, A. P. H. J. Humidity-responsive liquid crystalline polymer actuators with an asymmetry in the molecular trigger that bend, fold, and curl. *J. Am. Chem. Soc*. **136**, 10585-10588 (2014).

23. Wang, Z. *et al.* Reprogrammable humidity-driven liquid crystalline polymer actuator enabled by dynamic ionic bonds. *ACS Appl. Mater. Interfaces* **14**, 17869-17877 (2022).

24. Lan, R. *et al.* Reversibly and irreversibly humidity-responsive motion of liquid crystalline network gated by SO_2 gas. *Adv. Funct. Mater*. **29**, 1900013 (2019).

25. Hu, W. *et al.* Humidity-responsive blue phase liquid-crystalline film with reconfigurable and tailored visual signals. *Adv. Funct. Mater*. **30**, 2004610 (2020).

26. Liu, Y. *et al.* Humidity-and photo-induced mechanical actuation of cross-linked liquid crystal polymers. *Adv. Mater.* **29**, 1604792 (2017).

27. Zheng, X. *et al.* A Cut-and-Weld Process to 3D Architectures from Multiresponsive Crosslinked Liquid Crystalline Polymers. *Small* **15**, 1900110 (2019).

28. Wani, O. M., Verpaalen, R., Zeng, H., Priimagi, A. & Schenning, A. P. H. J. An artificial nocturnal flower via humidity-gated photoactuation in liquid crystal networks. *Adv. Mater.* **31**, 1805985 (2019).

29. Sun, H., Chai, X., Yang, H., Wei, J. & Yu, Y. Photo-and humidity-responsive liquid crystal copolymer actuators fabricated via vapor-assisted alignment. *ACS Appl. Mater. Interfaces* **16**, 15405-15415 (2024).

30. Sydney Gladman, A., Matsumoto, E. A., Nuzzo, R. G., Mahadevan, L. & Lewis, J. A. Biomimetic 4D printing. *Nat. Mater.* **15**, 413-418 (2016).

31. Zhu, Q. L. *et al.* Light-steered locomotion of muscle-like hydrogel by self-coordinated shape change and friction modulation. *Nat. Commun.* **11**, 5166 (2020).

32. Liu, M. *et al.* An anisotropic hydrogel with electrostatic repulsion between cofacially aligned nanosheets. *Nature* **517**, 68-72 (2015).

33. Wu, L. *et al.* Magnetically induced anisotropic orientation of graphene oxide locked by in situ hydrogelation. *ACS Nano* **8**, 4640-4649 (2014).

ARTICLE IN PRESS

ARTICLE IN PRESS

34. Zhu, Z. *et al.* Tough and thermosensitive poly (N-isopropylacrylamide)/graphene oxide hydrogels with macroscopically oriented liquid crystalline structures. *ACS Appl. Mater. Interfaces* **8**, 15637-15644 (2016).

35. Qin, H., Zhang, T., Li, N., Cong, H.-P. & Yu, S.-H. Anisotropic and self-healing hydrogels with multi-responsive actuating capability. *Nat. Commun.* **10**, 2202 (2019).

36. Yang, X. *et al.* Ordered gelation of chemically converted graphene for next-generation electroconductive hydrogel films. *Angew. Chem. Int. Ed.* **50**, 7325-7328 (2011).

37. Choi, S., Choi, Y. & Kim, J. Anisotropic hybrid hydrogels with superior mechanical properties reminiscent of tendons or ligaments. *Adv. Funct. Mater.* **29**, 1904342 (2019).

38. Lin, P., Zhang, T., Wang, X., Yu, B. & Zhou, F. Freezing molecular orientation under stretch for high mechanical strength but anisotropic hydrogels. *Small* **12**, 4386-4392 (2016).

39. Ye, S., Ma, W. & Fu, G. Anisotropic hydrogels constructed via a novel bilayer-co-gradient structure strategy toward programmable shape deformation. *Chem. Mater.* **35**, 999-1007 (2023).

40. Li, J. *et al.* Highly bidirectional bendable actuator engineered by LCST–UCST bilayer hydrogel with enhanced interface. *ACS Appl. Mater. Interfaces* **12**, 55290-55298 (2020).

41. Wu, S. *et al.* Aggregation-induced emissive carbon dots gels for octopus-inspired shape/color synergistically adjustable actuators. *Angew. Chem. Int. Ed.* **60**, 21890-21898 (2021).

42. Takahashi, R. *et al.* Control superstructure of rigid polyelectrolytes in oppositely charged hydrogels via programmed internal stress. *Nat. Commun.* **5**, 4490 (2014).

43. Kim, D. S., Lee, Y.-J., Kim, Y. B., Wang, Y. & Yang, S. Autonomous, untethered gait-like synchronization of lobed loops made from liquid crystal elastomer fibers via spontaneous snap-through. *Sci. Adv.* **9**, eadh5107 (2023).

44. Dhar, M., Das, A., Parbat, D. & Manna, U. Designing a network of crystalline polymers for a scalable, nonfluorinated, healable and amphiphobic solid slippery interface. *Angew. Chem.* **134**, e202116763 (2022).

45. Sarma, H. et al. Highly Water-Rich Robust Coating for Separating Immiscible Liquids Mixtures of wide Range of Surface Tension Differences. *Adv. Funct. Mater*. **34**, 2403607 (2024).

46. Liu, Z. et al. Multiple hydrogen-bonded cross-linked photo-responsive liquid crystal elastomers with photo-responsive fluorescence. *Polym*er **215**, 123420 (2021).

47. Gao, H. *et al.* Adaptive and freeze-tolerant heteronetwork organohydrogels with enhanced mechanical stability over a wide temperature range. *Nat. commun.* **8**, 15911 (2017).

ARTICLE IN PRESS

ARTICLE IN PRESS

48. Rather, A. M. et al. Color morphing surfaces with effective chemical shielding. *Nat. Commun*. **15**, 3735 (2024).

49. Sun, L. et al. Bioinspired programmable wettability arrays for droplet manipulation. *Proc. Natl. Acad. Sci. USA* **117**, 4527-4532 (2020).

50. Yao, Y. et al. Wettability-based ultrasensitive detection of amphiphiles through directed concentration at disordered regions in self-assembled monolayers. *Proc. Natl. Acad. Sci. USA* **119**, e2211042119 (2022).

51. Ryu, M., Yoon, J., Chae, M., Chun, H. J. & amp; Lee, H. Multi-Level Wettability Patterned Porous Matrix for Advanced Optical Information Encryption. *Adv. Funct. Mater.* **35**, 2414242 (2025).

52. Yu, B., Hu, H., Li, J., Ding, X. & amp; Li, Z. Wetting-Enabled Microfluidic Surface for Fluid/Droplet Manipulation: Fabrication, Strategies, and Applications. *Adv. Eng. Mater.* **26**, 2400200 (2024).

53. Wang, Z., Boechler, N. & Cai, S. Anisotropic mechanical behavior of 3D printed liquid crystal elastomer. *Addit. Manuf.* **52**, 102678 (2022).

54. Terentjev, E. M. Liquid crystal elastomers: 30 years after. *Macromolecules* **58**, 2792–2806 (2025).

55. Speregen, J. M. & White, T. J. Liquid crystalline elastomers in soft robotics: assessing promise and limitations. *Adv. Robot. Res.*, e202500150 (2025).

56. Barnes, M., Cetinkaya, S., Ajnsztajn, A. & Verduzco, R. Understanding the effect of liquid crystal content on the phase behaviour and mechanical properties of liquid crystal elastomers. *Soft Matter* **18**, 5074–5081 (2022).

57. Cang, Y., Liu, J., Ryu, M., Graczykowski, B., Morikawa, J., Yang, S. & Fytas, G. On the origin of elasticity and heat conduction anisotropy of liquid crystal elastomers at gigahertz frequencies. *Nat. Commun.* **13**, 5248 (2022).

58. Merkel, D. R., Traugutt, N. A., Visvanathan, R., Yakacki, C. M. & Frick, C. P. Thermomechanical properties of monodomain nematic main-chain liquid crystal elastomers. *Soft Matter* **14**, 6024-6036 (2018).

59. Okamoto, S., Sakurai, S. & Urayama, K. Effect of stretching angle on the stress plateau behavior of main-chain liquid crystal elastomers. *Soft Matter* **17**, 3128–3136 (2021).

ARTICLE IN PRESS

ARTICLE IN PRESS

60. Yang, R. & Zhao, Y. Non-uniform optical inscription of actuation domains in a liquid crystal polymer of uniaxial orientation: an approach to complex and programmable shape changes. *Angew. Chem.* **129**, 14390-14394 (2017).

61. Roach, D. J. et al. Long liquid crystal elastomer fibers with large reversible actuation strains for smart textiles and artificial muscles. *ACS Appl. Mater. Interfaces* **11**, 19514-19521 (2019).

62. Xiao, M., Xian, Y. & Shi, F. Precise macroscopic supramolecular assembly by combining spontaneous locomotion driven by the Marangoni effect and molecular recognition. *Angew. Chem. Int. Ed.* **54**, 9070–9074 (2015).

63.Yu, H., Wang, Y., Hou, Z., Xia, X., Chen, H., Zou, B. & Zhang, Y. Marangoni effect enabling autonomously miniatured swimmers: mechanisms, design strategy, and applications. *Adv. Funct. Mater.* **35**, e202424235 (2025).

64. Bormashenko, E., Frenkel, M., Bormashenko, Y., Chaniel, G., Valtsifer, V. & Binks, B. P. Superposition of translational and rotational motions under self-propulsion of liquid marbles filled with aqueous solutions of camphor. *Langmuir* **33**, 13184–13189 (2017).

65. Bormashenko, E., Bormashenko, Y., Grynyov, R., Aharoni, H., Whyman, G. & Binks, B. P. Self-propulsion of liquid marbles: Leidenfrost-like levitation driven by Marangoni flow. *J. Phys. Chem. C.* **119**, 9910−9915 (2015).

66. Ooi, C. H., Van Nguyen, A., Evans, G. M., Gendelman, O., Bormashenko, E. & Nguyen, N. T. A floating self-propelling liquid marble containing aqueous ethanol solutions. *RSC Adv.* **5**, 101006−101012 (2015).

67. Barman, N., Jain, K.; Borbora, A., Kumar, S., Tenjimbayashi, M., Manna, U. Regulating the self-propulsion of liquid marbles on a water pool. *Adv. Funct. Mater.* e05295 (2025).

68. Merkel, D. R., Traugutt, N. A., Visvanathan, R., Yakacki, C. M. & Frick, C. P. Thermomechanical properties of monodomain nematic main-chain liquid crystal elastomers. *Soft Matter* **14**, 6024-6036 (2018).

69. Barnes, M. & Verduzco, R. Direct shape programming of liquid crystal elastomers. *Soft Matter* **15**, 870-879 (2019).

70. Yakacki, C. M. *et al.* Tailorable and programmable liquid-crystalline elastomers using a two-stage thiol–acrylate reaction. *RSC Adv.* **5**, 18997-19001 (2015).

ARTICLE IN PRESS

71. Yang, R. & Zhao, Y. Non-uniform optical inscription of actuation domains in a liquid crystal polymer of uniaxial orientation: an approach to complex and programmable shape changes. *Angew. Chem.* **129**, 14390-14394 (2017).

72. Bauman, G. E., McCracken, J. M. & White, T. J. Actuation of liquid crystalline elastomers at or below ambient temperature. *Angew. Chem. Int. Ed.* **61**, e202202577 (2022).

73. Zhao, Y. *et al.* Double cross-linked biomimetic hyaluronic acid-based hydrogels with thermo-stimulated self-contraction and tissue adhesiveness for accelerating post-wound closure and wound healing. *Adv. Funct. Mater.* **33**, 2300710 (2023).

74. Mandal, S., Vignesh, A., Debnath, S. & Ojha, U. Mechanically robust anisotropic hydrogel–organogel conjugates for soft actuators with fast response time and diverse bi-axial programmable folding ability. *Chem. Mater.* **34**, 5125-5137 (2022).

75. Mahajan, A., Singh, A., Datta, D. & Katti, D. S. Bioinspired injectable hydrogels dynamically stiffen and contract to promote mechanosensing-mediated chondrogenic commitment of stem cells. *ACS Appl. Mater. Interfaces* **14**, 7531-7550 (2022).

76. Li, T. *et al.* Ultrastable piezoelectric biomaterial nanofibers and fabrics as an implantable and conformal electromechanical sensor patch. *Sci. Adv.* **10**, eadn8706 (2024).

ARTICLE IN PRESS

Acknowledgments

U.M. acknowledges generous financial support from Anusandhan National Research Foundation (CRG/2022/000710; SERB) and the Ministry of Electronics and Information Technology (no. 5(1)/2022-NANO). We acknowledge the generous support from Prof. E. Bhoje Gowd in performing WAXS. U.M. thanks the Department of Chemistry, Centre for Nanotechnology, Central Instrumental Facility, Indian Institute of Technology, Guwahati. P.G. thanks MoE and the institute for his doctoral fellowship.

Authors Contributions

PG performed all the experiments with the help of AB, DS, SD, AHW, HS, and AM. PG and AB designed experiments and analyzed data together. UM conceived the idea, UM and XW supervised

ARTICLE IN PRESS

the work together, UM wrote the manuscript, and all authors contributed to editing and reviewing the manuscript.

Competing interests

The authors have no competing interests to declare.

ARTICLE IN PRESS

Tables

Table 1: Accounting for the details of components to prepare BALCEH, maintaining different compositions of hydrogel and LCE networks.

RM257 (mg)	HDDA (mg)	Photo initiator (HMP) (mg)	PETMP (mg)	TEA (mg)	5CB (mg)	Weight ratio hydrogel: LCE
42.5	2.5	5	5	2	15	1:1
51	3	5	6	2	15	1:1.2
59.5	3.5	5	7	2	15	1:1.4
63.5	4	5	7.5	3	15	1:1.5
74	4.5	5	9	3	15	1:1.75

Figure Captions

Fig. 1: Synthesis and characterization of bicontinuous LCE–hydrogel (BALCEH). Molecular

ARTICLE IN PRESS

structures of chemicals used to prepare **a** the hydrogel network: N,N-dimethylacrylamide (DMA) and N,N′-methylenebis(acrylamide) (BIS), and **b** the LCE network: reactive mesogen 1,4-bis-[4-(3-acryloyloxypropyloxy)benzoyloxy]-2-methylbenzene) (RM257), non-mesogenic diacrylate spacer 1,6-hexanediol diacrylate (HDDA), and crosslinker pentaerythritol tetrakis(3-mercaptopropionate) (PETMP). **c** Schematic illustration of the stepwise fabrication of the BALCEH double network: where a hydrogel scaffold was fabricated prior to infusion of required ingredients (RM257 and HDDA) into it via swelling, and followed by thiol Michael addition reaction between thiol and acrylate moieties. Thereafter, the photopolymerization of residual acrylates under uniaxial mechanical strain (for uniaxially aligned BALCEH). **d** ATR–FTIR spectra of the hydrogel (blue), precursor-infused hydrogel (orange), and BALCEH (cyan) showing characteristic spectral transitions during network formation. **e** Raman spectral mapping across the cross-section of BALCEH demonstrates uniform distribution of characteristic functional groups (C–H, C=O, aromatic C=C, N–H, C–S, C–N). Blue, red and black lines indicate the top, interior and bottom location, respectively. **f** Polarized optical microscopy (POM) images of uniaxially aligned (top) and non-aligned (bottom) BALCEH sample. Double-headed arrows indicating orientation of the cross-polarizer; ‘n’ denotes the director, and single headed arrow shows the direction of alignment. **g** The Wide-angle X-ray scattering (WAXS) represented with 2D profile of BALCEH (top) and its analogues having LCE polydomain (bottom). *S* denotes the orientational order parameter. **h, i** Accounting corresponding q-space scan (**h**) and azimuthal profiles for respective samples (**i**).

Fig. 2: Adaptive and extreme surface wettability of LCE–hydrogel (BALCEH). a Digital image of the hydrogel showing underwater superoleophobicity for a beaded DCE droplet (dyed with Nile Red, top) and underoil (heptane) water infiltration (bottom). Water was dyed with Methylene blue. **b** Digital images of LCE showing high oleophilicity underwater (top) and superhydrophobicity underoil (bottom). **c** Plot accounting for the impact of the relative content of hydrogel and LCE in the prepared BALCEH on both oil and water wettability in submerged conditions. BALCEH with hydrogel: LCE weight ratio of 1:1.5 displayed both underwater superoleophobicity and underoil superhydrophobicity (marked with dotted box). **d** Digital images of BALCEH displaying both superoleophobicity underwater (top) and superhydrophobicity underoil (bottom). **e** Schematic depicting BALCEH equilibrated and submerged in water (left)

ARTICLE IN PRESS

and oil (right). Depending on the exposures of selected liquids, either hydrogel or LCE networks dominate and contribute to respective extreme liquid (oil/water) repellence. **f** Digital images of BALCEH after being submerged and equilibrated in water (left) and oil (right). **g** Raman spectra of hydrogel, LCE, and BALCEH after equilibration with water and heptane, and **h** corresponding 2D Raman mapping for dry BALCEH and after separately equilibrated with water and oil. **i** Schematic depicting the spatial reconfiguration of the constituent networks of BALCEH when equilibrated with different solvent environments. Data are presented as mean values ± standard deviation (SD). The error bar indicates SD with number of measurements, n= 3 for each data point. Source data are provided as a Source Data file.

Fig. 3: Anisotropic mechanical properties of BALCEH: a The plot accounting for the mechanical properties (Young's modulus and modulus of toughness) of BALCEH, LCE and hydrogel. **b** Digital images showing the survival of BALCEH under twisting, folding, and creasing. **c** Digital image demonstrating the ability of BALCEH to lift a load of 500 times its own weight. Data are presented as mean values ± standard deviation (SD). The error bar indicates the SD with number of measurements, n=3 for each data point. The bar height represents the mean value for Young's modulus measurement. Source data are provided as a Source Data file.

Fig. 4: Stimuli-responsive, reversible deformations of LCE–hydrogel (BALCEH). a An arc-shaped hydrogel strip shows irreversible actuation, whereas **b** an arc-shaped LCE shows no actuation in water. **c** A preprogrammed arc-shaped BALCEH strip gradually relaxes when immersed in water and returns to its original shape upon ambient drying. L represents the end-to-end distance of the arc-shaped strip, and α is the angle between L and the vertical axis. **d** Accounting curvature evolution with time for arc-shaped BALCEH (black), hydrogel (blue) and LCE (orange) and analogue of BALCEH (green) with polydomain LCE on submerging under water (open circles) and in drying condition (close circles). R^2 represents the coefficient of determination for the fitted data. **e, f** Bright-field (left) and cross-polarized (right) optical microscopic images showing time-resolved anisotropic swelling under water (**e**) and de-swelling in ambient (**f**), it expands and shrinks orthogonal to the LCE director. Double-headed arrows indicating orientation of the cross-polarizer; 'n' denotes the director, and single headed arrow shows the direction of alignment. **g** Schematic illustrating the actuation mechanism: hydrogel swelling induces a tension force that drives gradual unfurling in water or water-miscible solvents, while the elastic restoring force from the uniaxially aligned LCE promotes shape recovery during

ARTICLE IN PRESS

deswelling. **h** Humidity-triggered reversible shape transformation of a helically shaped BALCEH strip (RH represents relative humidity). **i** Temperature-responsive, reversible contraction and elongation of a BALCEH strip.

Fig. 5: Bio-inspired autonomous locomotion of solvent-soaked LCE–hydrogel (BALCEH). a Schematic illustrating natural surfactant-induced autonomous motion of a rove beetle at the air-water interface. **b** Time-lapse images showing circular locomotion of a rectangular-shaped BALCEH soaked with ethanol on a circular water pool. **c** The plot accounting for the motion trajectory of ethanol-soaked LCE (red), hydrogel (blue), and BALCEH (grey) over time on the pool. **d** Plot depicting the quenching of self-propulsion of BALCEH strip upon external addition of ethanol to the water pool. **e** IR-thermograph of the motion for BALCEH strip on a water pool (white dotted circle represents the boundary of water pool). M_1, M_2 and M_3 denotes location of measured temperatures on self-propelled BALCEH, water pool and surrounding of water pool. **f** Plot comparing motion duration and efficiency of various solvents (denoted as fuel) for self-propulsion of BALCEH. **g** The plot accounting for the periodic motion (circular and halt) upon repetitive external addition of toluene to the water pool. Data are presented as mean values ± standard deviation (SD). Bar height represents the mean value and the error bar indicates SD with number of measurements, n=3 for each data point. Source data are provided as a Source Data file.

Fig. 6: Controlled modulation of the motion trajectory. a Time-lapse images of a 3D-printed triangular swimmer (orange) attached with ethanol-soaked BALCEH (schematically shown at top) on a water pool during its autonomous locomotion and the corresponding motion trajectory profile. **b** The time-lapse digital images and plot accounting transition in trajectory from circular (red line in the plot) to rotary (orange line in the plot) of an actuating 3D-printed swimmer (orange part in the images) decorated with two rectangular-shaped BALCEH strips loaded with ethanol and DCE (dyed with Nile red). **c** Schematic depicting a plausible mechanism for the transition of motion trajectory based on the choice of fuels. **d** Plot depicting the motion trajectory transition of a 3D-printed swimmer attached with two BALCEH strips loaded with two different fuels (ethanol and DCE) upon external addition of toluene to the water pool during its self-propulsion. Red, black and orange lines indicate circular, halt and rotary motion, respectively. **e** Time-resolved images showing the bending angle change of the arc-shaped BALCEH with time upon water absorption. β defines the bending angle. **f** Overall motion profile showing a vortex-like outward spiral motion

ARTICLE IN PRESS

trajectory of a 3D printed swimmer. Green, cyan and blue lines indicate the initial, intermediate and final stages of the motion, respectively. **g** Plot accounting for the change of diameter of circular path of 3D-printed swimmer as a function of change in bending angle of the arc-shaped navigation tail. Green and blue shades indicate transition from initial to final stages of the motion. Data are presented as mean values ± standard deviation (SD). The error bar indicates the SD with number of measurements, n=3 for each data point. Source data are provided as a Source Data file.

ARTICLE IN PRESS

ARTICLE IN PRESS

Editorial Summary
It is challenging to achieve both reversible shape reconfiguration and autonomous motion with a synthetic soft material. Here, the authors report the development of an elastomer-hydrogel composite that shows both behaviours as a result of asymmetric solvent uptake.

Peer review information: *Nature Communications* thanks Wei Feng, Fuhua Xue, and the other, anonymous, reviewer for their contribution to the peer review of this work. A peer review file is available.

ARTICLE IN PRESS

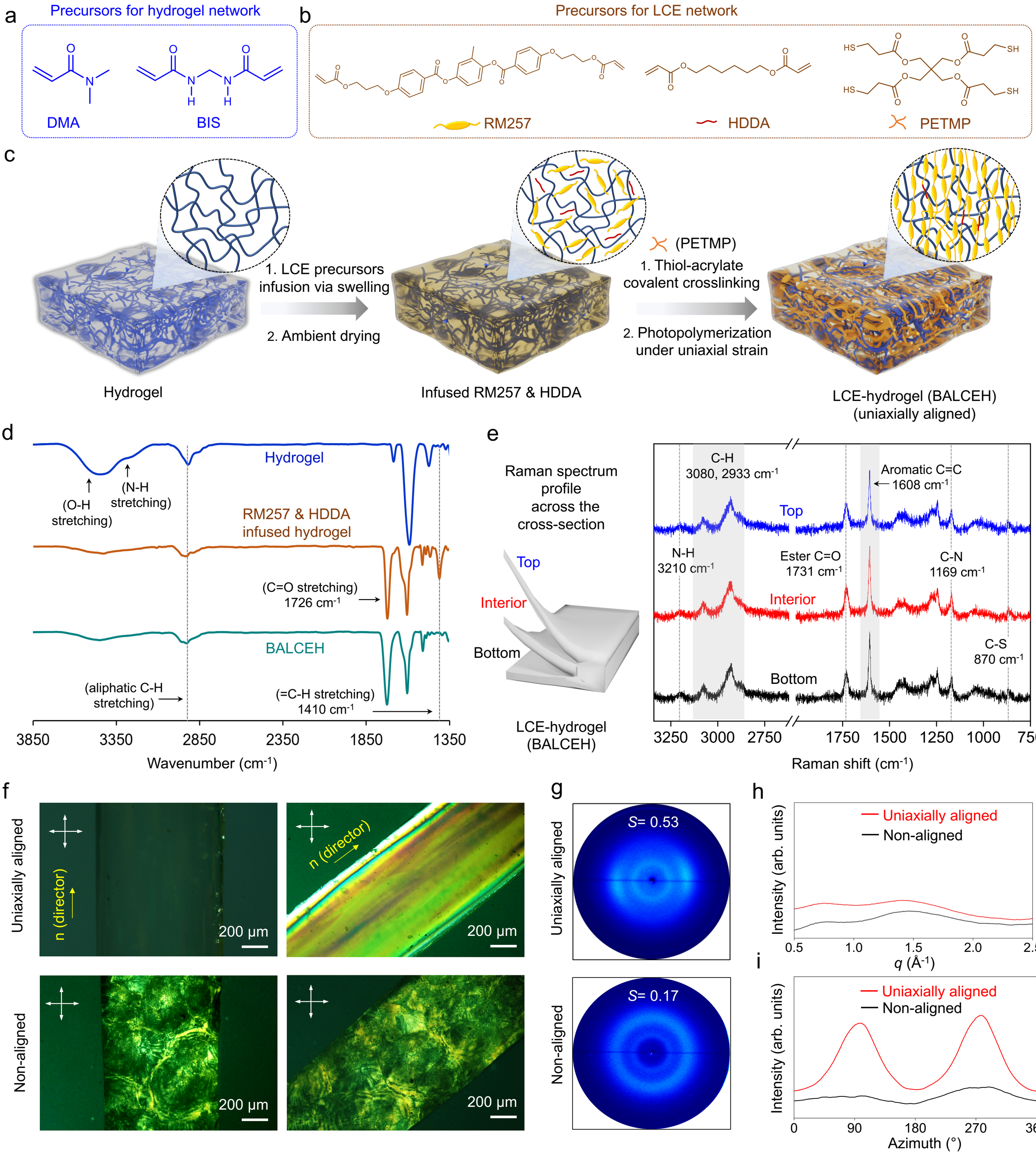
a
Precursors for hydrogel network
DMA
BIS
b
Precursors for LCE network
RM257
HDDA
PETMP
c
1. LCE precursors infusion via swelling
2. Ambient drying
(PETMP)
1. Thiol-acrylate covalent crosslinking
2. Photopolymerization under uniaxial strain
Hydrogel
Infused RM257 & HDDA
LCE-hydrogel (BALCEH) (uniaxially aligned)
d
Hydrogel
(O-H stretching)
(N-H stretching)
RM257 & HDDA infused hydrogel
(C=O stretching) 1726 cm-1
BALCEH
(aliphatic C-H stretching)
(=C-H stretching) 1410 cm-1
3850
3350
2850
2350
1850
1350
Wavenumber (cm-1)
e
Raman spectrum profile across the cross-section
Top
Interior
Bottom
LCE-hydrogel (BALCEH)
C-H 3080, 2933 cm-1
Aromatic C=C 1608 cm-1
Top
N-H 3210 cm-1
Ester C=O 1731 cm-1
C-N 1169 cm-1
Interior
C-S 870 cm-1
Bottom
3250
3000
2750
1750
1500
1250
1000
750
Raman shift (cm-1)
f
Uniaxially aligned
n (director)
200 μm
Non-aligned
g
Uniaxially aligned
S= 0.53
Non-aligned
S= 0.17
h
Uniaxially aligned
Non-aligned
Intensity (arb. units)
0.5
1.0
1.5
2.0
2.5
q (Å-1)
i
Uniaxially aligned
Non-aligned
Intensity (arb. units)
0
90
180
270
360
Azimuth (°)

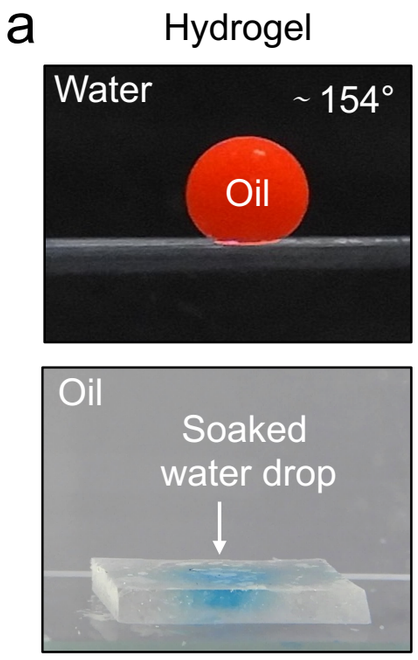
a
Hydrogel
Water
~ 154°
Oil
Oil
Soaked
water drop

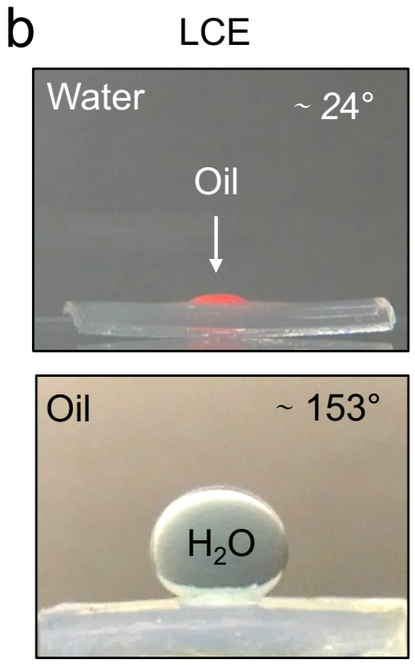
b
LCE
Water
~ 24°
Oil
Oil
~ 153°
H2O

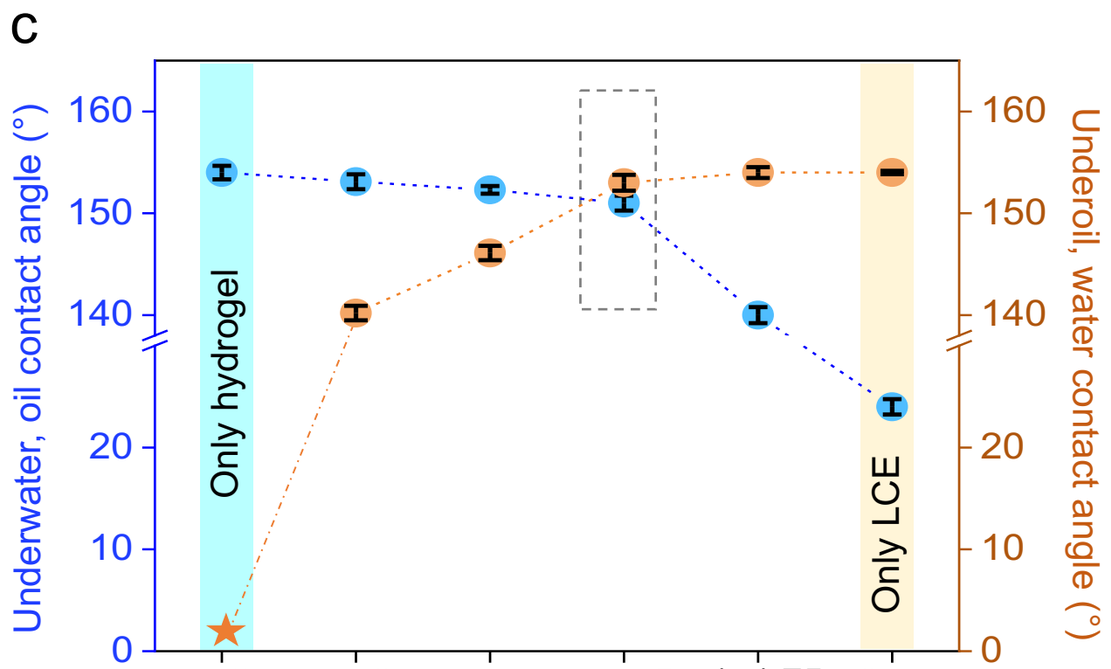
c
Underwater, oil contact angle (°)
Underoil, water contact angle (°)
Only hydrogel
Only LCE
160
150
140
20
10
0
1: 0
1: 1.2
1: 1.4
1: 1.5
1: 1.75
0: 1
Hydrogel: LCE (weight ratio)

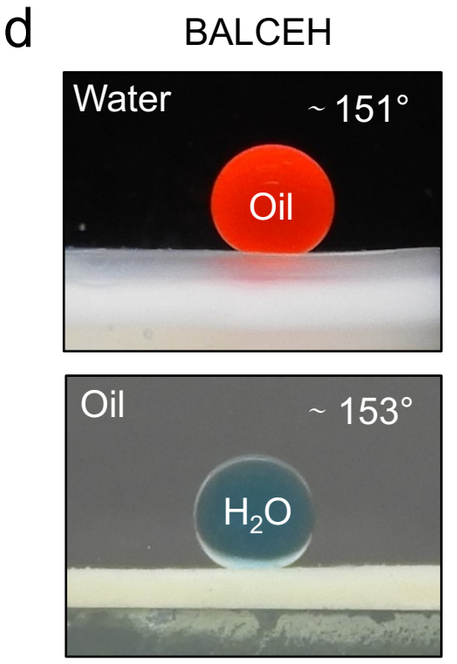
d
BALCEH
Water
~ 151°
Oil
Oil
~ 153°
H2O

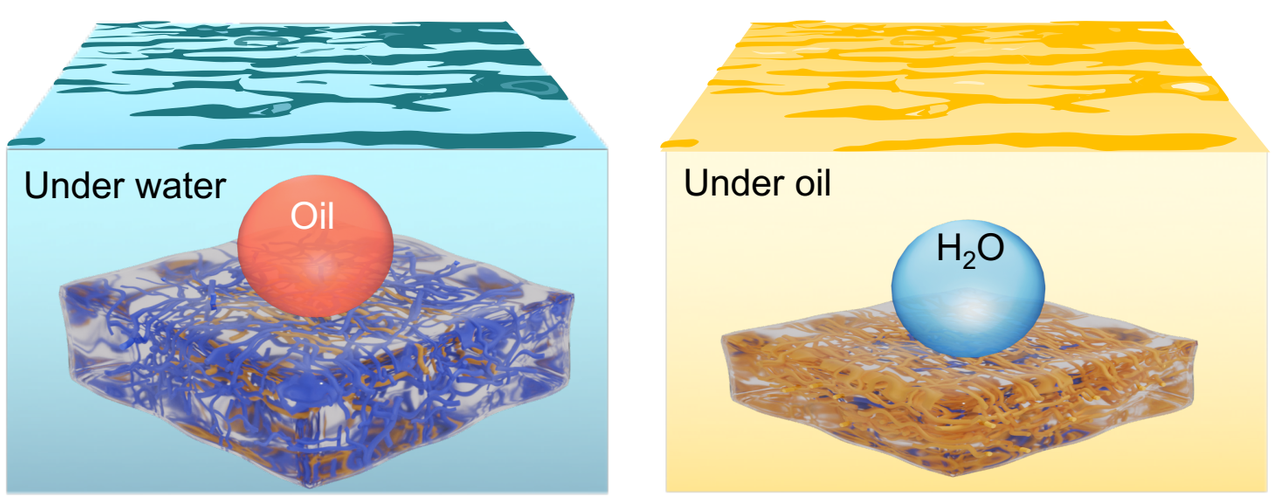
e
Under water
Oil
Under oil
H2O

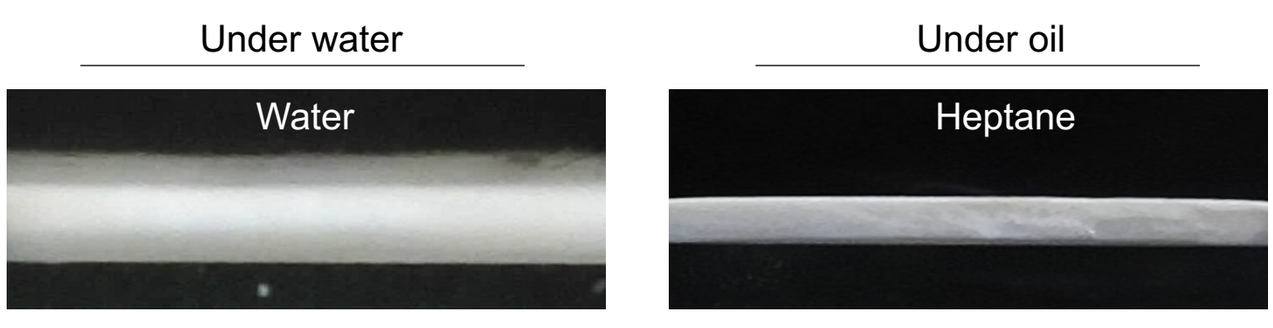
f
Under water
Water
Under oil
Heptane

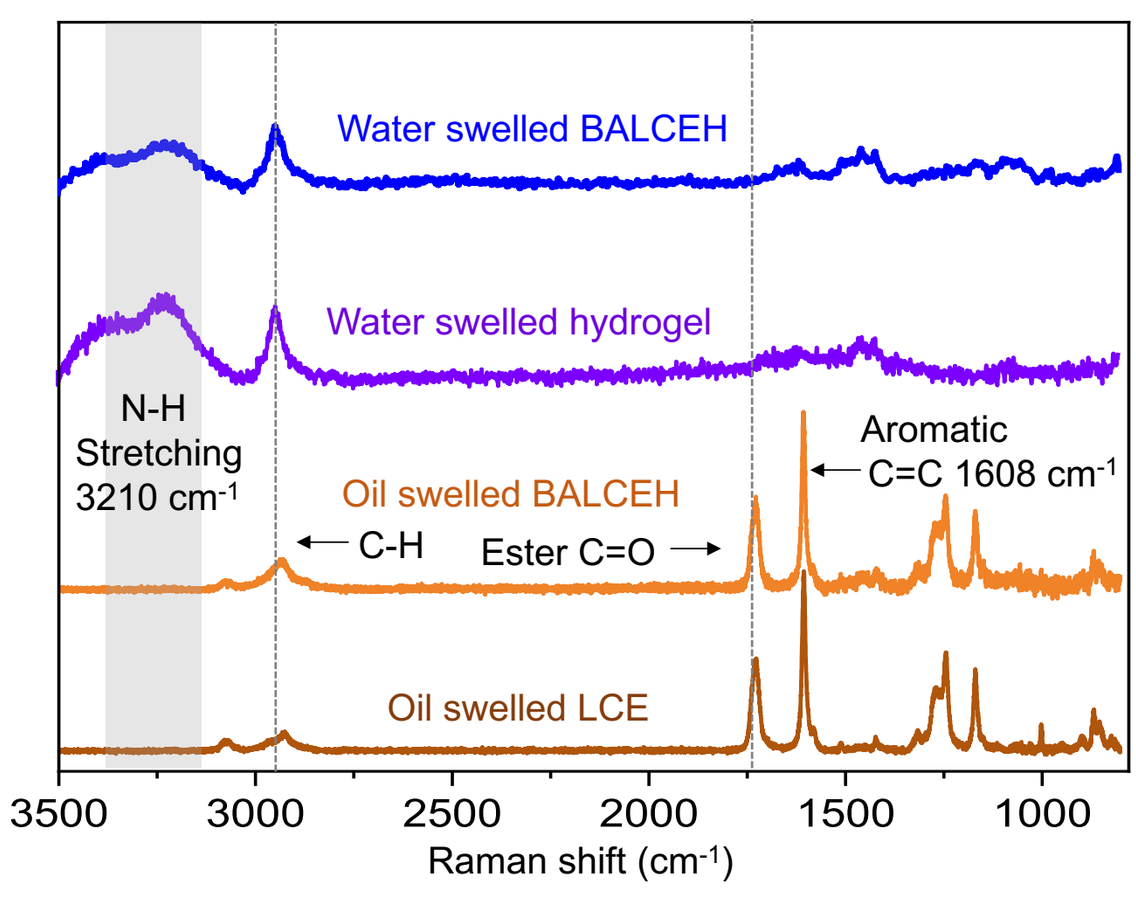
g
Water swelled BALCEH
Water swelled hydrogel
N-H
Stretching
3210 cm-1
Aromatic
C=C 1608 cm-1
Oil swelled BALCEH
C-H
Ester C=O
Oil swelled LCE
3500
3000
2500
2000
1500
1000
Raman shift (cm-1)

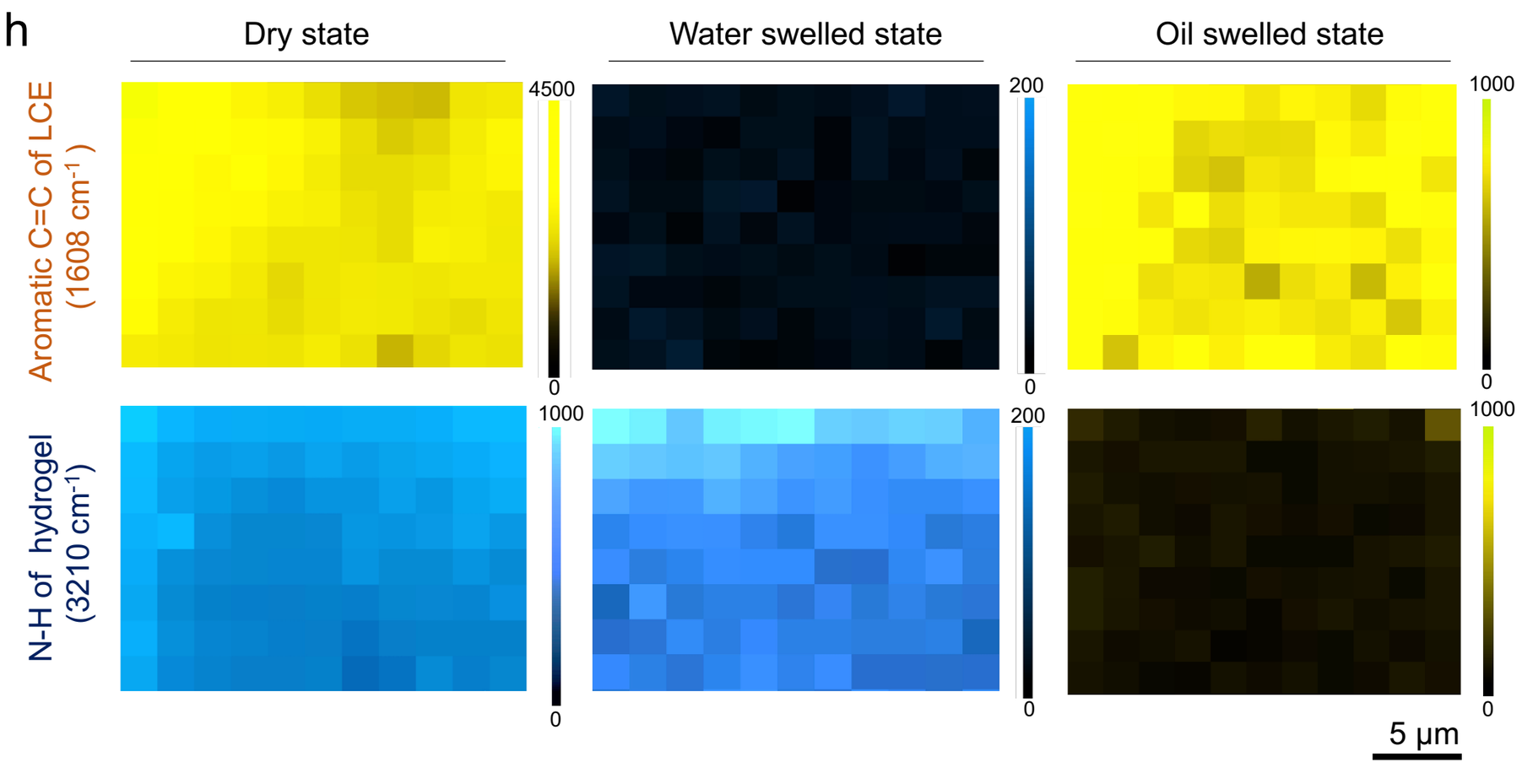
h
Dry state
Water swelled state
Oil swelled state
Aromatic C=C of LCE
(1608 cm-1)
N-H of hydrogel
(3210 cm-1)
4500
0
200
0
1000
0
1000
0
200
0
1000
0
5 μm

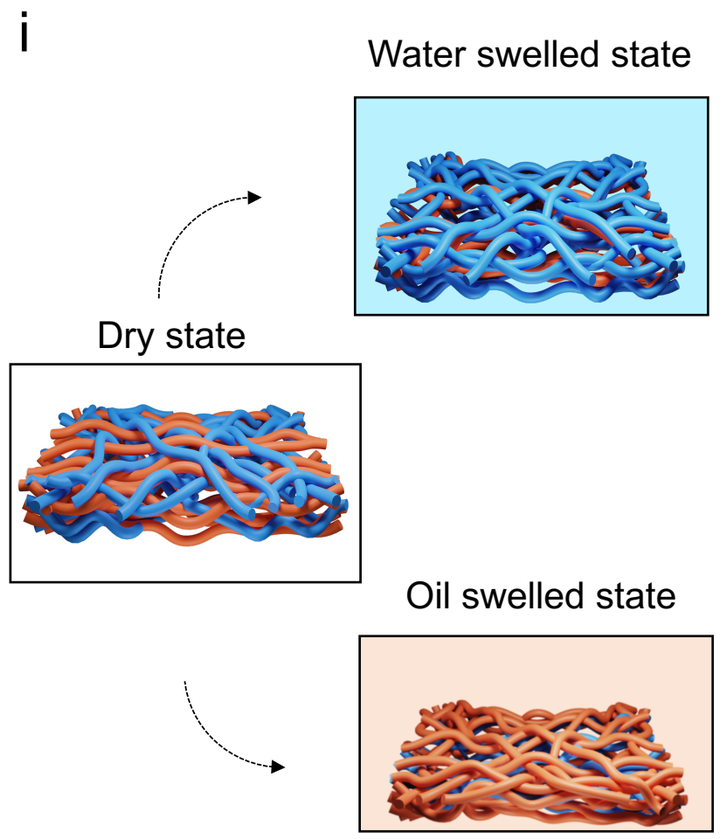
i
Water swelled state
Dry state
Oil swelled state

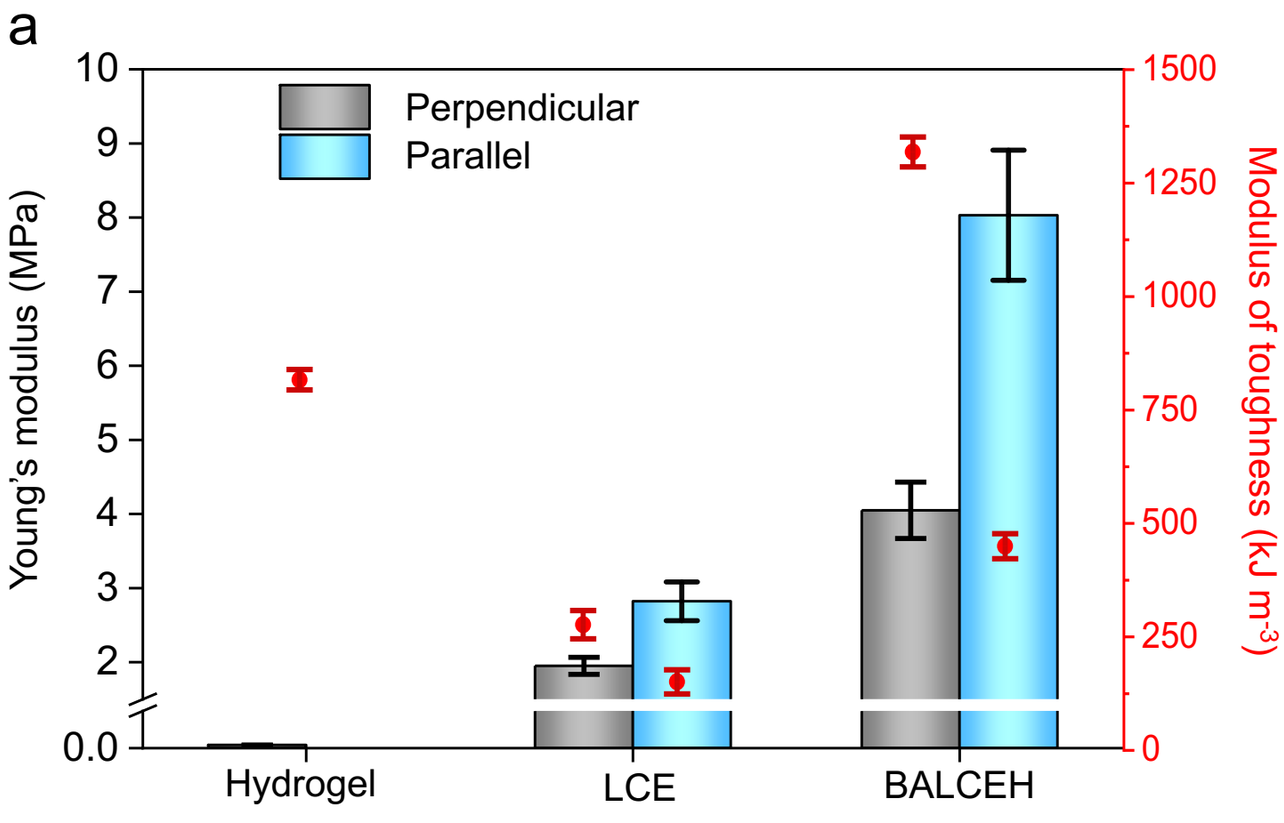
a
Young's modulus (MPa)
Modulus of toughness (kJ m-3)
Perpendicular
Parallel
10
9
8
7
6
5
4
3
2
0.0
1500
1250
1000
750
500
250
0
Hydrogel
LCE
BALCEH

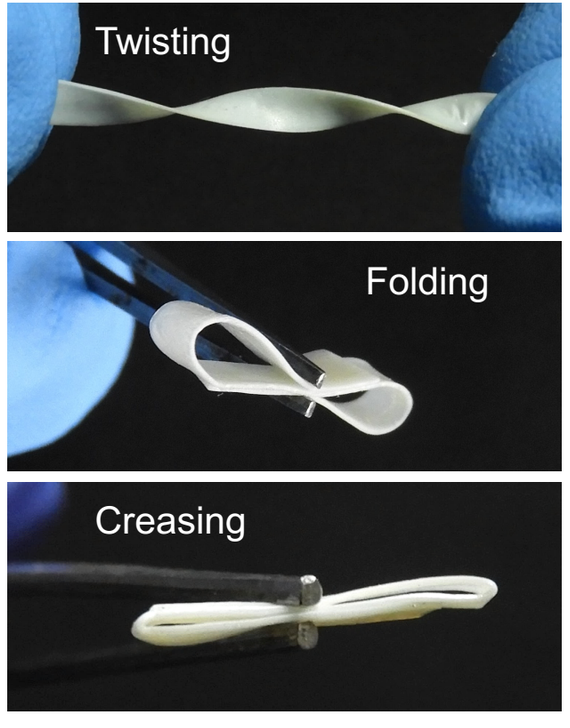
b
Twisting
Folding
Creasing

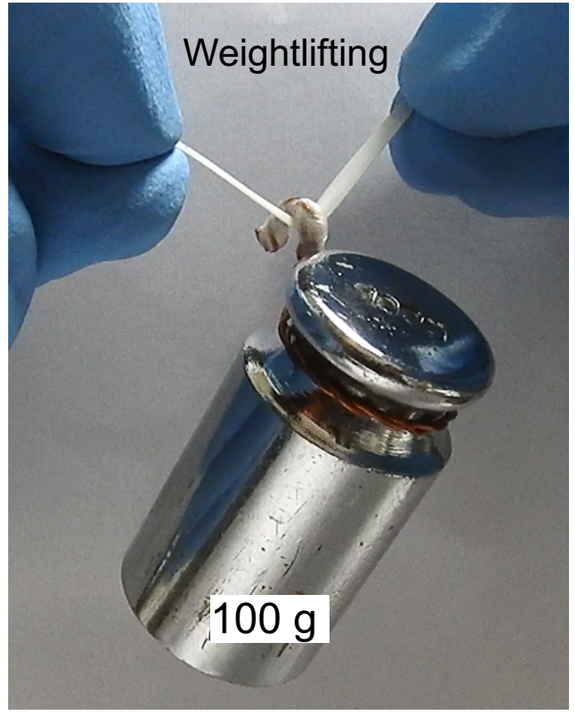
c
Weightlifting
100 g

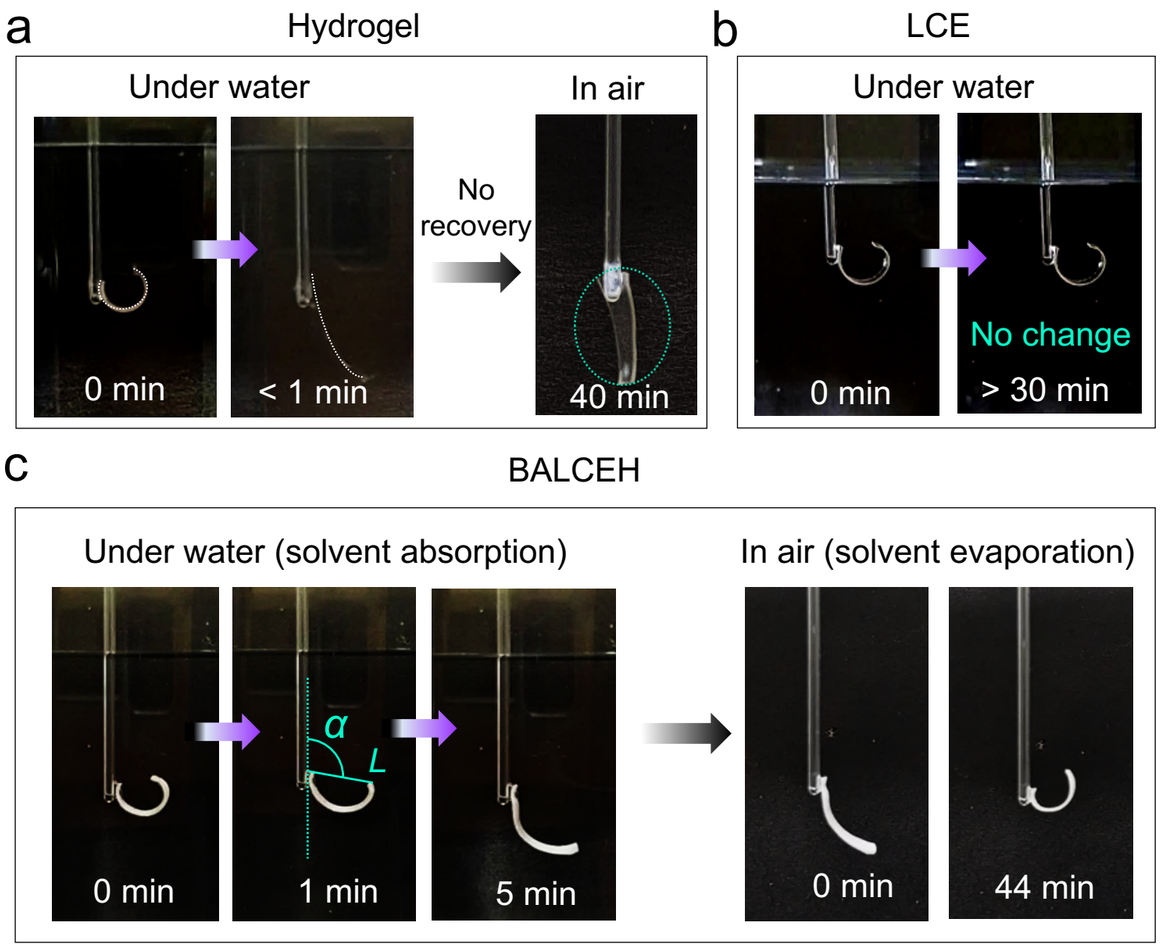
a
Hydrogel
Under water
In air
No recovery
0 min
< 1 min
40 min
b
LCE
Under water
No change
0 min
> 30 min
c
BALCEH
Under water (solvent absorption)
In air (solvent evaporation)
α
L
0 min
1 min
5 min
0 min
44 min

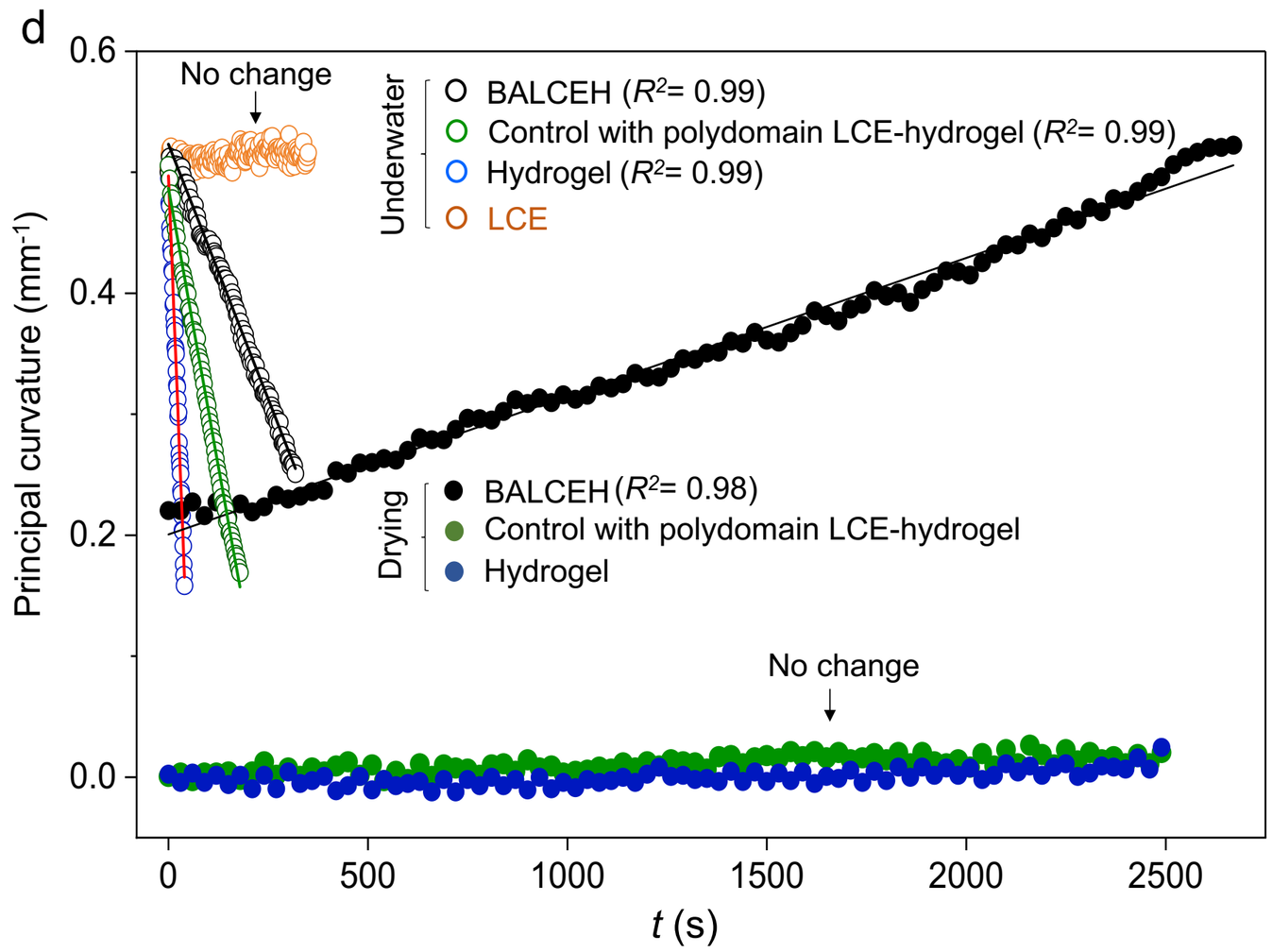
d
Principal curvature (mm-1)
0.6
0.4
0.2
0.0
No change
Underwater
BALCEH (R2= 0.99)
Control with polydomain LCE-hydrogel (R2= 0.99)
Hydrogel (R2= 0.99)
LCE
Drying
BALCEH (R2= 0.98)
Control with polydomain LCE-hydrogel
Hydrogel
No change
0
500
1000
1500
2000
2500
t (s)

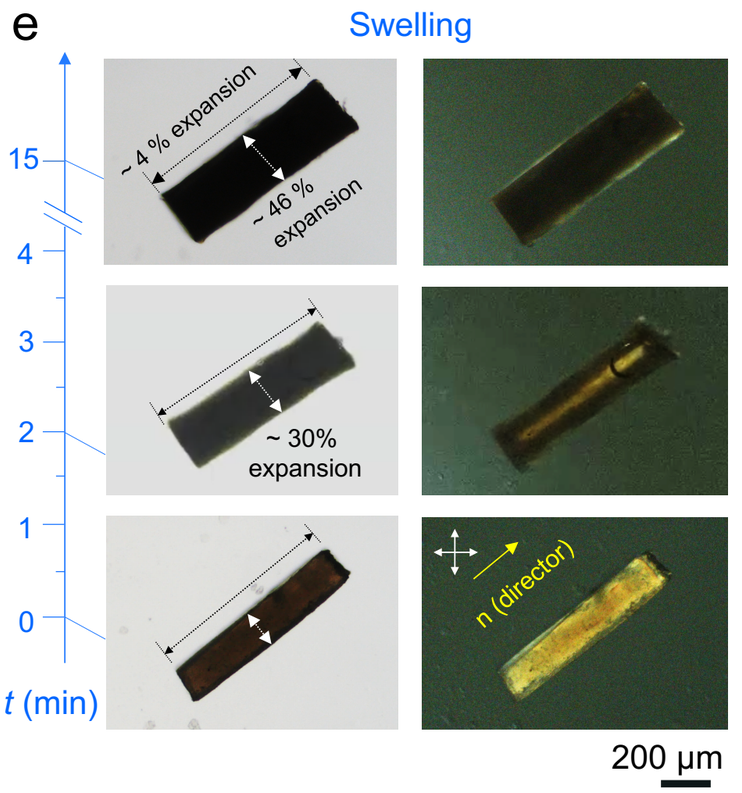
e
Swelling
15
4
3
2
1
0
t (min)
~ 4 % expansion
~ 46 % expansion
~ 30% expansion
n (director)
200 μm

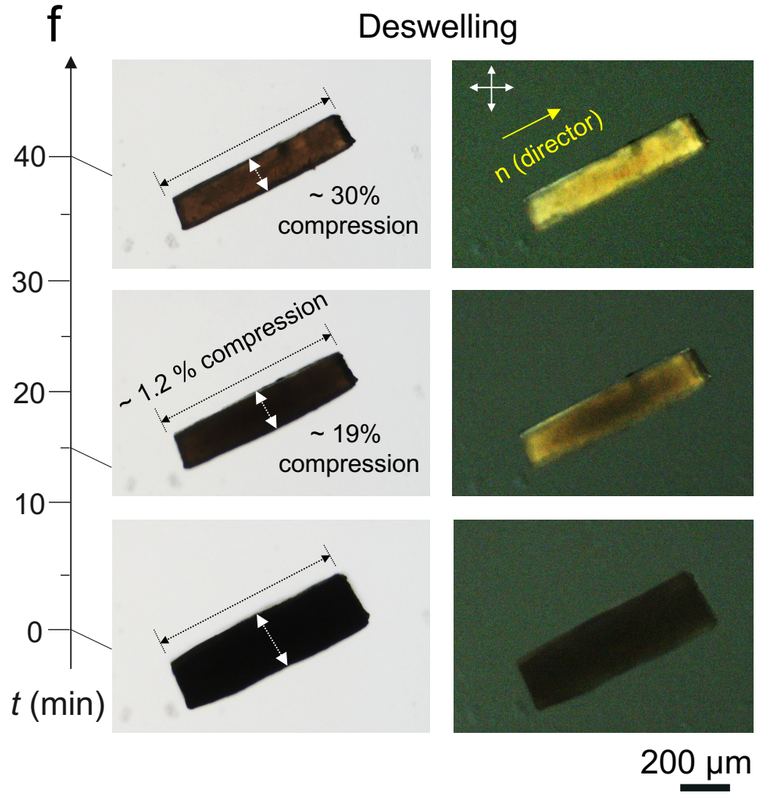
f
Deswelling
40
30
20
10
0
t (min)
~ 30% compression
n (director)
~ 1.2 % compression
~ 19% compression
200 μm

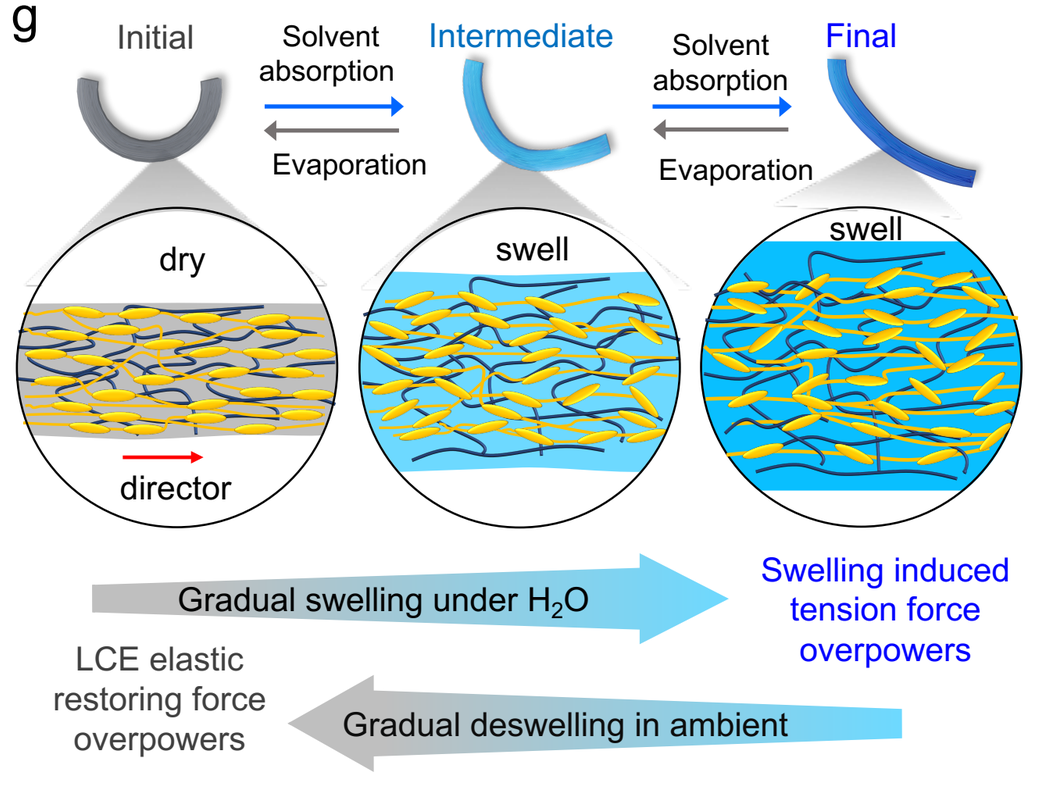
g
Initial
Solvent absorption
Evaporation
Intermediate
Solvent absorption
Evaporation
Final
dry
director
swell
swell
Gradual swelling under H2O
Swelling induced tension force overpowers
LCE elastic restoring force overpowers
Gradual deswelling in ambient

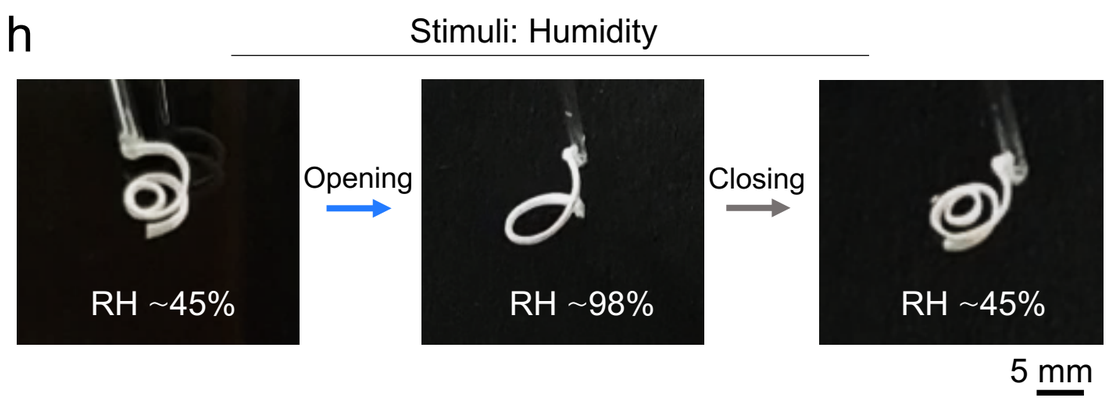
h
Stimuli: Humidity
RH ~45%
Opening
RH ~98%
Closing
RH ~45%
5 mm

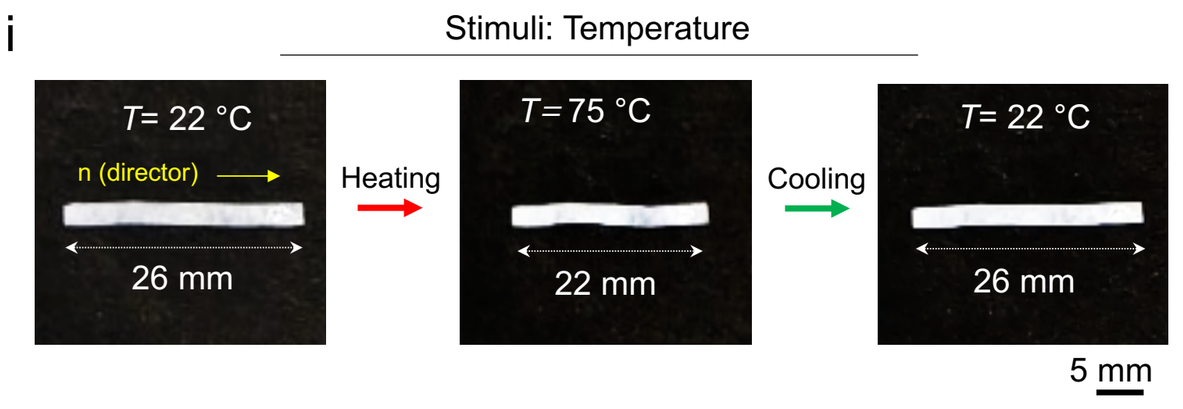
i
Stimuli: Temperature
T= 22 °C
n (director)
26 mm
Heating
T= 75 °C
22 mm
Cooling
T= 22 °C
26 mm
5 mm

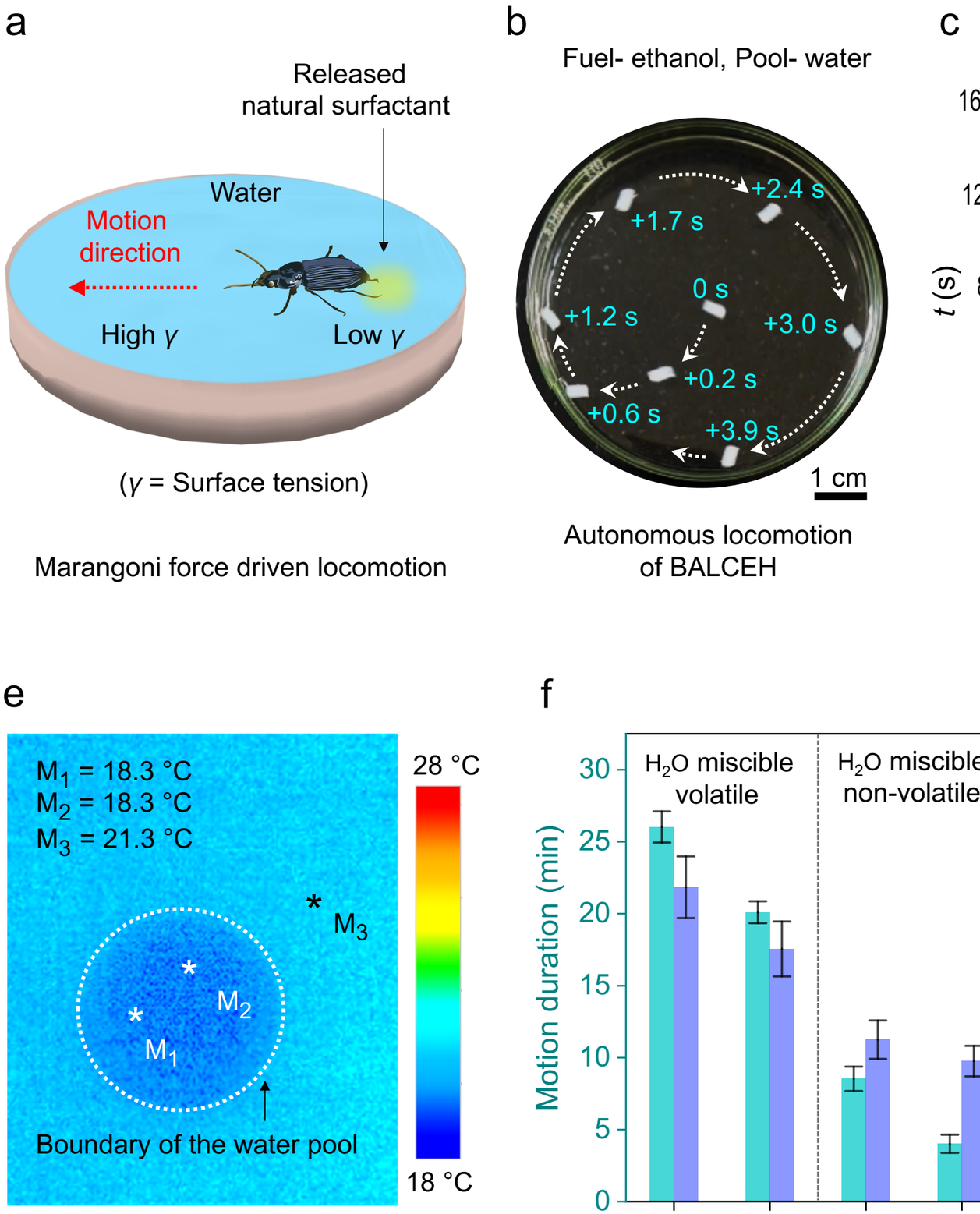
a
Released
natural surfactant
Water
Motion
direction
High γ
Low γ
(γ = Surface tension)
Marangoni force driven locomotion
b
Fuel- ethanol, Pool- water
+2.4 s
+1.7 s
0 s
+1.2 s
+3.0 s
+0.2 s
+0.6 s
+3.9 s
1 cm
Autonomous locomotion
of BALCEH
c
Fuel- ethanol
Hydrogel
LCE
BALCEH
1600
1200
800
400
0
t (s)
X (cm)
Y (cm)
d
Quenching
upon
ethanol addition
300
200
100
0
t (s)
X (cm)
Y (cm)
e
M1 = 18.3 °C
M2 = 18.3 °C
M3 = 21.3 °C
M3
M2
M1
Boundary of the water pool
28 °C
18 °C
f
H2O miscible
volatile
H2O miscible
non-volatile
H2O immiscible
volatile
Motion duration (min)
Fuel efficiency (min mg-1)
Ethanol
ACN
DMF
DMSO
DCE
Ethyl ether
g
Halt
Halt
Halt
X (cm)
Circular
Circular
Circular
Circular
t (s)

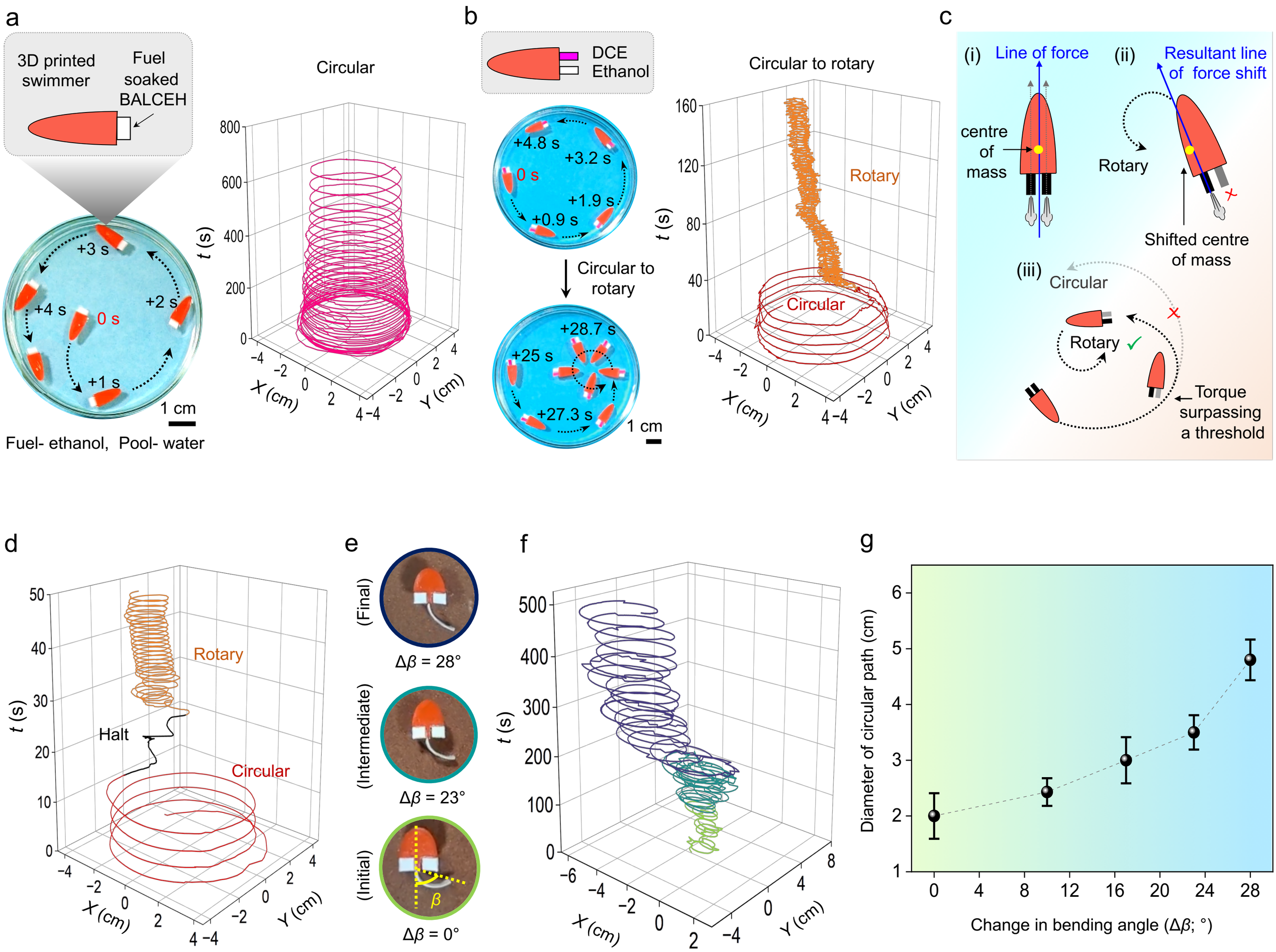
a
3D printed swimmer
Fuel soaked BALCEH
+3 s
+2 s
+4 s
0 s
+1 s
1 cm
Fuel- ethanol, Pool- water
Circular
t (s)
X (cm)
Y (cm)
b
DCE
Ethanol
+4.8 s
+3.2 s
0 s
+1.9 s
+0.9 s
Circular to rotary
+28.7 s
+25 s
+27.3 s
1 cm
Circular to rotary
Rotary
Circular
c
(i) Line of force
centre of mass
(ii) Resultant line of force shift
Rotary
Shifted centre of mass
(iii)
Circular
Rotary
Torque surpassing a threshold
d
Rotary
Halt
Circular
e
(Final)
Δβ = 28°
(Intermediate)
Δβ = 23°
(Initial)
β
Δβ = 0°
f
g
Diameter of circular path (cm)
Change in bending angle (Δβ; °)